JOURNAL OF PETROLOGY | VOLUME 39 | NUMBER 1 | PAGES 61–99 | 1998

High *P–T* Polymetamorphism, Dehydration Melting, and Generation of Migmatites and Granites in the Higher Himalayan Crystalline Complex, Sikkim, India

SUDIPTA NEOGI[1], SOMNATH DASGUPTA[2]* AND MASATO FUKUOKA[3]

[1]GEOLOGICAL SURVEY OF INDIA, CENTRAL PETROLOGICAL LABORATORIES, 15 KYD STREET, CALCUTTA-700 016, INDIA

[2]DEPARTMENT OF GEOLOGICAL SCIENCES, JADAVPUR UNIVERSITY, CALCUTTA-700 032, INDIA

[3]DEPARTMENT OF EARTH AND PLANETARY SCIENCES, HIROSHIMA UNIVERSITY, HIGASHI-HIROSHIMA, JAPAN

RECEIVED NOVEMBER 25, 1996; REVISED TYPESCRIPT ACCEPTED JULY 24, 1997

The Higher Himalayan Crystalline Complex (HHC) in Sikkim, India, consists of pelitic migmatites interlayered with calc-silicate rocks and minor metabasites. Microstructural relationships between the mineral phases and deformational fabric elements and zoning characteristics of garnet indicate a prolonged and complex polymetamorphic history for the HHC. The pelitic rocks in the upper part of the HHC contain the assemblage plagioclase + quartz ± garnet + K-feldspar + biotite + sillimanite and are devoid of muscovite. Most of the mineral phases grew syn- to post-tectonically. Mineral growth coincided with development of a pervasive fabric (S_2) during prograde metamorphism (M_2), in the early stages of the collisional event. Some garnet grains display texturally distinct cores and rims, which are separated by calcic plagioclase. This texture suggests an earlier metamorphic episode (M_1). M_1 may represent pre-Himalayan metamorphism and decompression of the HHC. Later, the collisional event led to renewed burial of the HHC and M_2 reactions. M_2 is reflected by dehydration melting of muscovite and biotite to form granitic melts, which either crystallized in situ *to form leucosomes, or migrated from their source regions to form larger granitic bodies. Geothermobarometric estimates for peak M_2 conditions indicate P = 10–12 kbar, T = 800–850°C. A subsequent metamorphic event (M_3) occurred because of ~5 kbar of decompression. M_3 is recorded by the breakdown of porphyroblastic garnet in all HHC lithologies. Higher temperature and pressure estimates come from progressively higher structural levels of the complex. The thermal gradient of 5·5°C/km is anomalous, and may be a consequence of thermal buffering during melting. However, the pressure gradient of 0·25 kbar/km resembles a normal lithostatic gradient, which suggests that the HHC in Sikkim represents an inverted Barrovian sequence. This inverted zonation of the HHC is probably the result of large-scale structural inversion and/or tectonic juxtaposition because of ductile shearing.*

KEY WORDS: *dehydration melting; high-grade polymetamorphism; inverted metamorphism; Sikkim Himalayas*

INTRODUCTION

The tectonothermal evolution of the Himalayas reflects events that accompanied collision of the Indian and Eurasian plates during the Eocene (~50 Ma). This continent collision resulted from the closure of the Neo-Tethys and the subduction of the Indian plate below Tibet. The >2500 km of post-Eocene shortening has been mainly accommodated through crustal stacking, along a system of intracontinental thrusts and internal deformation of the Indian plate (Patriat & Achache, 1984; Molnar, 1986).

The major controversies concerning the *P–T* evolution of the Himalayas revolve around (1) heat source of

*Corresponding author.

© Oxford University Press 1998

metamorphism, (2) the nature and origin of inverted metamorphism, (3) the ages of metamorphic and deformational events, and (4) the relationships among metamorphism, deformation, and magmatism (see for review, Barnicoat & Treloar, 1989; Swapp & Hollister, 1991; Hodges *et al.*, 1994; Grujik *et al.*, 1996; Parrish & Hodges, 1996). Very different *P–T* paths are reported from various parts of the Himalayas. One reason for this variation may be that thermal regimes may differ along the vast length of the orogenic belt, but a major factor appears to be different interpretations of the deformational and metamorphic histories. For example, although a Himalayan age for the main penetrative fabric is suggested on the basis of mineral ages (Brunel & Kienast, 1986; Hodges & Silverberg, 1988; Hodges *et al.*, 1988; Pecher, 1989; Wheeler *et al.*, 1995), a pre-collisional age has also been proposed (Reddy *et al.*, 1993). Barrovian style inverted metamorphism has been reported throughout the Himalayas (Oldham, 1883; Ray, 1947; Gansser, 1964, 1983; Le Fort, 1975; Honegger *et al.*, 1982; Banerjee *et al.*, 1983; Brunel & Kienast, 1986; Hodges *et al.*, 1988; Hubbard, 1989; Pecher, 1989; Searle & Rex, 1989; Staubli, 1989; Treloar *et al.*, 1989, among others). A sequence of progressively higher-grade rocks occurs at higher structural levels in the Lesser Himalayas and the Main Central Thrust (MCT) zone (references as above). The picture in the Higher Himalayas is rather confusing, because both increasing (e.g. Metcalf, 1993) and decreasing (Thakur, 1986; Lombardo *et al.*, 1993) grades towards higher structural levels have been described. Numerous models have been proposed to account for the observed inverse metamorphic zonation in the Himalayas. These include (1) thrusting of a hot slab over a cold one [the 'hot-iron' model of Le Fort (1975)], (2) shear heating along thrusts (England & Molnar, 1993), (3) post-metamorphic imbricate thrusting (Treloar *et al.*, 1989), (4) post-metamorphic folding of the isograds (Searle & Rex, 1989), (5) tectonic juxtaposition of high- and low-grade rocks (Swapp & Hollister, 1991; Jain & Manickavasagam, 1993) and (6) syn-metamorphic ductile shearing (Grujik *et al.*, 1996; Jamieson *et al.*, 1996; Davidson *et al.*, 1997). A prominent role is assigned to the MCT in most of these models. It is generally regarded as a major intracrustal ductile thrust zone, a few kilometres wide (Grujik *et al.*, 1996). In some parts of the orogen, the upper bounding fault of the MCT zone marks a metamorphic discontinuity (Hodges & Silverberg, 1988; Metcalf, 1993), whereas in other parts no such break is recognized (e.g. Hubbard, 1989).

In this paper, we describe the petrology of the Higher Himalayan Crystalline Complex in Sikkim, eastern Himalaya. The present study focuses on the upper part of the Higher Himalayan slab, beginning at structural levels from which primary muscovite has been eliminated from the assemblages of pelitic rocks up to its northern contact with the Tethyan sedimentary sequence. We use the mineral assemblages, reaction textures and geothermobarometric estimates to demonstrate a complex polymetamorphic history for these rocks.

REGIONAL GEOLOGIC SETTING

Since the work of Gansser (1964) in Darjeeling–Sikkim, most workers have divided the Himalayas into a series of longitudinal tectonostratigraphic domains: (1) Sub Himalayas, (2) Lesser Himalayas, (3) Higher Himalayas, and (4) Tethys Himalayas (Fig. 1a), separated by major dislocation zones.

In the Sikkim region, units are disposed in an arcuate regional fold pattern (Fig. 1b). The 'core' of the region is occupied by the Lesser Himalayan low-grade metapelites (Daling Group, Proterozoic to Mesozoic) and the distal parts by medium- to high-grade crystalline rocks of the Higher Himalayan Belt (Higher Himalayan Crystalline Complex, HHC, Proterozoic?). A prominent ductile shear zone (the MCT) separates the two belts. In this region, the MCT is the southernmost of a number of northward-dipping ductile shear zones within the Higher Himalayan Crystalline Complex. Gondwana (Carboniferous–Permian) and molasse-type Siwalik (Miocene–Pliocene) sedimentary rocks of the Sub-Himalayan Zone occur in the southern part of the region. In the far north, a thick pile of Cambrian to Eocene fossiliferous sediments of the Tethyan Zone (Tethyan Sedimentary sequence, Fig. 1b) overlie the HHC on the hanging wall side of a series of north-dipping normal faults constituting the South Tibetan Detachment System (STDS; Burchfiel *et al.*, 1992).

The HHC consists predominantly of high-grade pelitic migmatites with subordinate calc-silicate rocks, metabasites and granites. The pelitic migmatites are stromatic, with layer-parallel granitic leucosomes and biotite-rich melanosomes (Fig. 2). Patchy leucosomes and discordant veins are also present (Fig. 3). Banded, finely foliated, and augen gneisses show transitions from stretched leucosomes to composite crystal augens with porphyroblasts of K-feldspar. The augen gneisses display pervasive mylonitic microfabrics, suggesting that augen development may reflect strain heterogeneities. These rocks all contain the same AFM phases and are inferred to have been derived from pelitic precursors. Numerous layers of calc-silicate rocks and minor quartzite occur throughout the HHC. Small bodies of metabasic rocks are generally conformable to the gneissic and migmatitic layering. Intrusive bodies of biotite and tourmaline leucogranites, rarely exceeding a few tens of metres, occur in great profusion in the upper parts of the HHC.

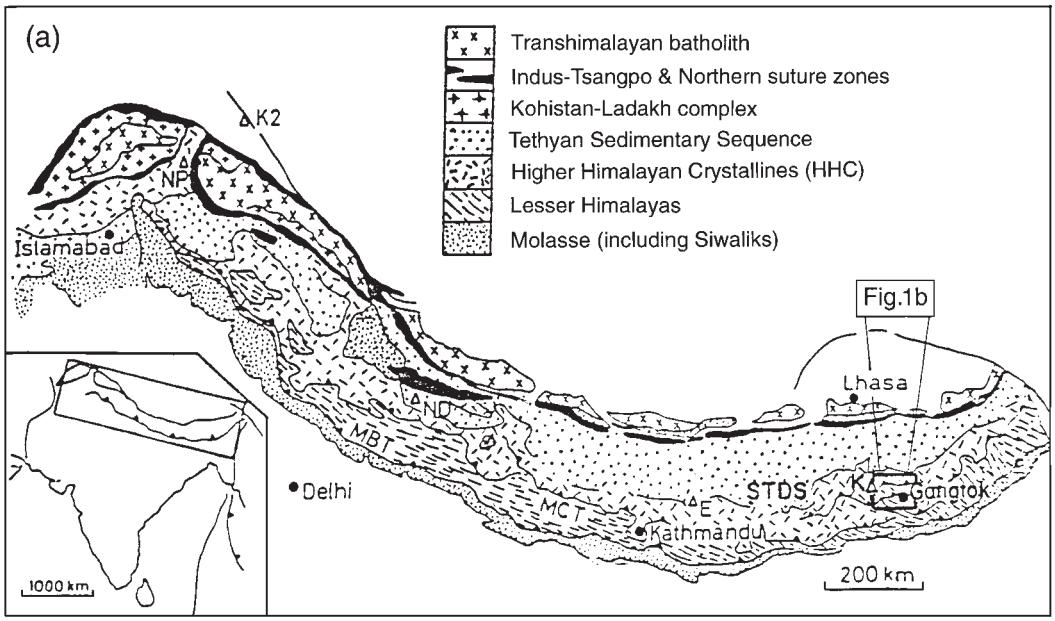

Fig. 1.

Structural studies of the Himalayas have reported a number of deformational events and related fabric elements (e.g. SinhaRoy, 1976; Brunel, 1986). The dominant structural element in the pelitic rocks is a penetrative foliation, designated here as S_2, because an earlier deformation is sporadically represented by an early fabric (S_1) that defines microfolds within the S_2-related layering or is seen as internal trails within syn-S_2 garnet porphyroblasts. S_2 is related to a set of locally preserved, rootless, isoclinal folds (F_2) seen in quartzofeldspathic layers. F_2 formed during the D_2 (Fig. 4). S_2 is commonly seen as a gneissic layering that is defined by the alignment of biotite and sillimanite grains. These mafic layers alternate with felsic ones that contain elongated and flattened grains of feldspar and quartz. The pelitic units also show a mylonitic microfabric (S_m) characterized by thin layers of fine-grained recrystallized quartz–feldspar aggregates which anastomose around or cut across porphyroclasts of feldspar and quartz. The S_m fabric intersects the S_2 fabric at low angles, which suggests that shearing may have been initiated early in the D_2 period and continued into the post-D_2 time. The most common folds (F_3) in the Higher Himalayan pelites, however, are those that involve S_2 folia. A weakly developed crenulation cleavage (S_3) is locally seen parallel to the axial planes of meso- and macro-scale F_3 folds and is marked by incipient growth of biotite and chlorite.

A number of discrete linear zones of ductile deformation (DDZ) are seen in many localities. The DDZ cut across lithological boundaries and the planar fabric S_2. These zones are narrow, characterized by intense mylonitization, formed late in the deformation history (post-D_2), and are associated with mineral lineations and stretching lineations. The stretching lineations generally plunge to the north. Shear sense indicators consistently indicate a top-to-the-south sense of movement. S–C fabrics associated with the north-to-south transport are found within the gneisses in these zones (Fig. 5).

PETROGRAPHY

Pelitic rocks

The pelitic migmatites are essentially composite in character, composed of quartzofeldspathic leucocratic regions with biotite-rich selvedges, which alternate with grey gneiss. Some patchy leucosomes and discordant veins (Fig. 3) contain cordierite. Locally, relicts of earlier generation of leucocratic regions occur as rootless isoclinal F_2 folds (Fig. 6).

Leucocratic regions

The leucocratic regions are granitic in composition and much coarser grained than the host gneiss. They contain varying proportions of quartz, K-feldspar and plagioclase, with minor sillimanite, muscovite, biotite and garnet. The leucocratic regions display simple hypidiomorphic textures. Aspect ratios of quartz and plagioclase are low (~2:1). Quartz occurs mostly as xenomorphic interstitial grains between coarser feldspar, or as drop-like inclusions within plagioclase. Plagioclase is coarse (~0·2–1·5 mm),

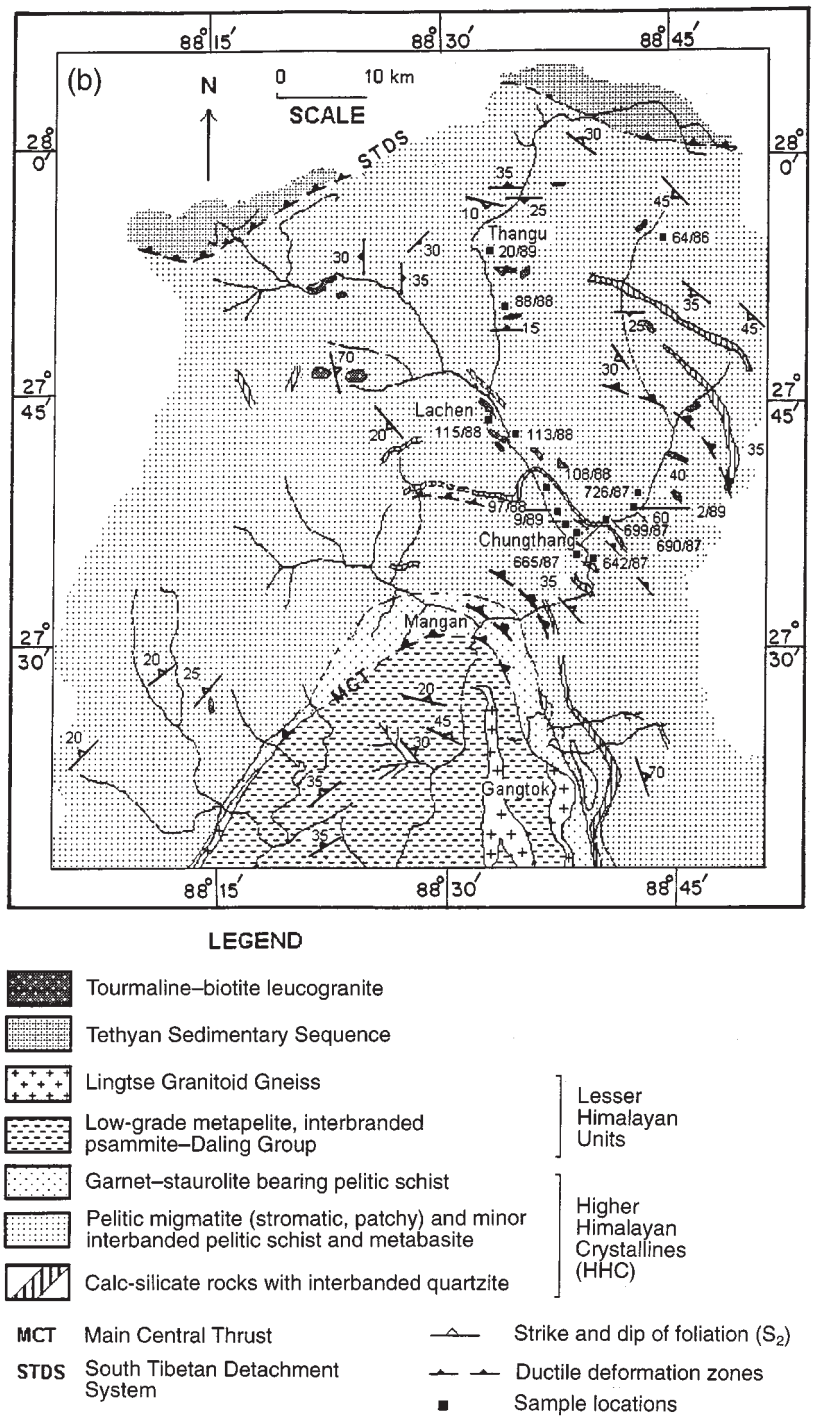

Fig. 1. (a) Generalized geological map of the Himalayas, showing the different geotectonic domains and lithounits [modified after Honegger *et al.* (1982)]. Inset shows the location of the Sikkim Himalayas. MBT, Main Boundary Thrust; NP, Nanga Parbat; ND, Nanda Devi. (b) Schematic geological map of the Sikkim Himalayas, showing the location of the samples.

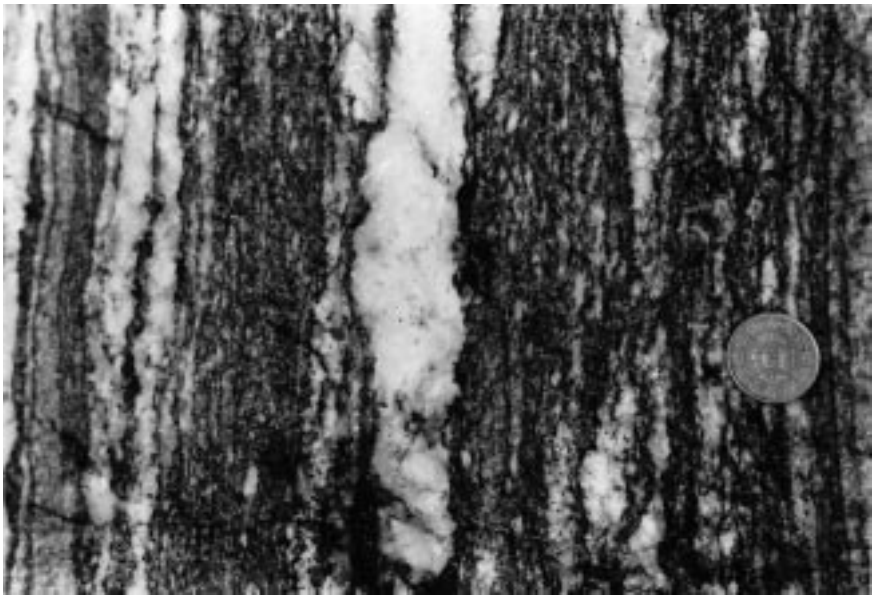

Fig. 2. Stromatic pelitic migmatite with discrete layer-parallel quartzofeldspathic leucocratic regions bordered by biotite-rich selvedge (melanosome) and a gneissic part.

Fig. 3. Discordant leucocratic veins cutting across the pervasive S_2 fabric and the layer-parellel leucocratic regions in pelitic migmatite.

subhedral, locally weakly deformed and ranges from albite to oligoclase in composition. Plagioclase is typically zoned, and the zone boundaries are distinctly idiomorphic. K-feldspar is present in variable amounts (up to 35 modal %) as xenoblastic grains, generally microperthitic. Biotite (greenish brown) may be present locally as randomly oriented flakes, with chloritic rims. Sillimanite needles are seen as isolated grains or as clusters within plagioclase grains. Garnet appears in significant proportions in some leucocratic regions at higher structural levels. Xenoblastic cordierite grains from thin leucosome veins contain inclusions of biotite grains. Zircon and apatite are minor accessory minerals.

Host gneiss

The host gneiss consists of biotite + quartz + plagioclase + K-feldspar + sillimanite + cordierite +

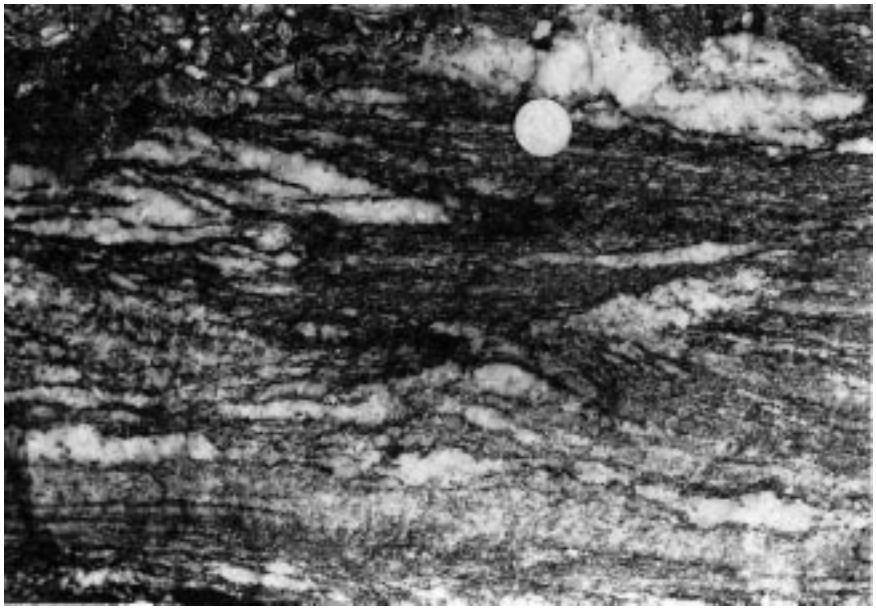

Fig. 4. Early rootless F_2 folds defined by quartzofeldspathic layers in pelitic migmatite. The S_2 fabric is axial planar to these folds.

ilmenite ± garnet ± spinel ± magnetite ± graphite ± apatite.

Biotite is generally mahogany-red in colour and occurs as fine flakes that define the S_2 foliation (along with sillimanite), or as poikiloblasts that have overgrown this fabric. The oriented flakes are likely to have grown syntectonically with S_2, but the poikiloblastic grains clearly indicate that biotite growth outlasted S_2. Quartz–biotite intergrowths (Fig. 7), and patchy secondary biotite + sillimanite, replace some garnet grains (Fig. 8). Sillimanite occurs as: (1) fibrous aggregates concentrated along the S_2 folia with biotite, (2) plicated masses forming intrafolial pods, or (3) coarse prisms derived from the coarsening of fibrolite needles.

Garnet found in pelitic rocks is commonly porphyroblastic, generally irregular shaped, locally displays rims, and varies in size from 0·4 mm to ~10 mm. These garnet grains generally lack any internal fabric; instead, they contain numerous inclusions in cores, and display inclusion-free rims. Typically, a break between cores and rims is defined by a ring of inclusions or a thin coating of plagioclase. Such garnets evidently grew in two stages, pre- to syntectonically and post-tectonically with the S_2-forming deformational event. Discrete post-S_2 garnet grains occur as highly sieved skeletal grains that have overgrown the matrix fabric (Fig. 9). Garnet coronas between sillimanite and plagioclase occur adjacent to leucocratic veins (Fig. 10).

Porphyroblastic K-feldspar is fairly abundant. Grains are typically perthitic, but some occur as intergrowths with quartz or as smaller interstitial grains along with plagioclase. Plagioclase grains are deformed, xenoblastic, generally untwinned, and locally myrmekitic. Cordierite occurs between garnet and biotite or sillimanite (Fig. 11). Spinel–quartz symplectites that rim sillimanite or garnet occur in the highest structural levels of the Higher Himalayan Crystalline Zone (Fig. 12a and b). Quartz is highly deformed. Locally, it forms ribbon-like grains with aspect ratios >10. Ilmenite is the most common opaque mineral in these rocks. It occurs as irregularly shaped grains or needles associated with the breakdown of biotite. Graphite grains are less commonly observed.

Calc-silicate rocks

The calc-silicate rocks can be grouped into two associations:

Type I: calcite + clinopyroxene$_1$ ± scapolite + plagioclase + quartz ± garnet + sphene ± clinopyroxene$_2$ ± plagioclase$_2$ ± epidote ± wollastonite (+ zoisite + hornblende ± tremolite) (the subscript 2 for clinopyroxene and plagioclase refers to symplectitic varieties described below);

Type II: epidote + quartz + clinopyroxene + garnet + plagioclase + sphene + calcite (+ hornblende + chlorite).

Type I is the dominant association. It is characterized by higher modal abundance of calcite relative to Type II and presence of scapolite. The granoblastic polygonal texture of these calc-silicate rocks is made up of a coarse mosaic of calcite, clinopyroxene$_1$ and plagioclase$_1$. Clinopyroxene is xenoblastic, and contains inclusions of plagioclase, sphene and calcite. Some clinopyroxene grains

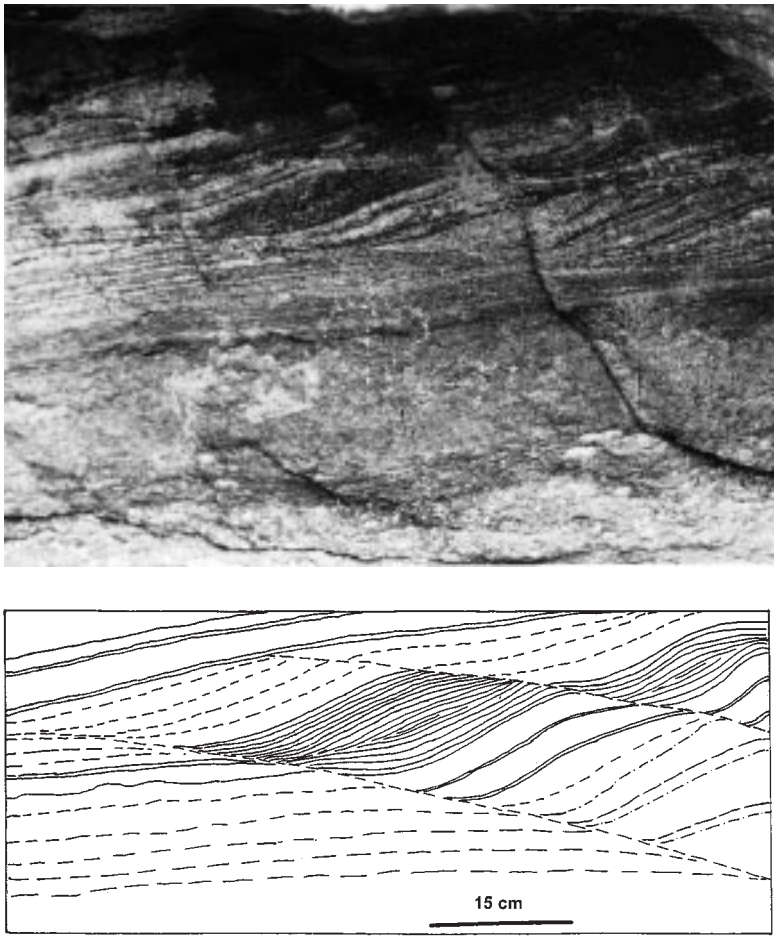

Fig. 5. S–C band structure developed in pelitic migmatite in ductile shear zones.

display amphibole rims. Matrix plagioclase$_1$ is xenoblastic and twinned. Garnet is porphyroblastic. It contains inclusions of quartz, plagioclase and, rarely, calcite. Some grains are rimmed by symplectites of clinopyroxene$_2$ and plagioclase$_2$ (Fig. 13). Scapolite occurs as partial pseudomorphs of plagioclase$_1$. Zoisite occurs as rims on clinopyroxene and scapolite or as partial replacements of plagioclase grains. Wollastonite has been detected in only one sample, where it occurs as xenoblastic grains.

Association Type II contains abundant epidote, but little calcite. Garnet occurs locally as lobate worm-like grains that contains inclusions of epidote.

Metabasic rocks

Both foliated and massive metabasic rocks occur in the HHC. Foliated metabasites are conformable with surrounding pelites. The foliation in the metabasites is defined by hornblende and ribbon-like aggregates of quartz and plagioclase. The metabasic rocks contain hornblende + plagioclase$_1$ + quartz + orthopyroxene + plagioclase$_2$ + clinopyroxene + garnet + opaques. Plagioclase$_2$ is the symplectitic variety, described below.

Amphibole is the dominant mafic phase in the metabasites. It occurs as prismatic grains of hornblende that are aligned with the foliation or anthophyllite replacement of orthopyroxene in orthopyroxene–plagioclase$_2$ symplectites around garnet grains. Plagioclase$_1$ occurs as interstitial grains in the matrix. Garnet is commonly xenoblastic and highly embayed. Garnet grains are rimmed by plagioclase$_2$ (Fig. 14). Some garnet porphyroblasts are surrounded by orthopyroxene–plagioclase$_2$ symplectites (Fig. 15), or by plagioclase$_2$–amphibole–quartz intergrowths. Composite garnet grains with texturally distinct 'cores' and 'rims' occur in the lower part of the crystalline complex in the study area (Fig. 16a and b). The core and rim sections are separated by plagioclase$_2$ and differ in their inclusion characteristics and zoning patterns, which are discussed in a later section. Both features indicate garnet growth during two distinct episodes. Cores of such grains contain randomly oriented

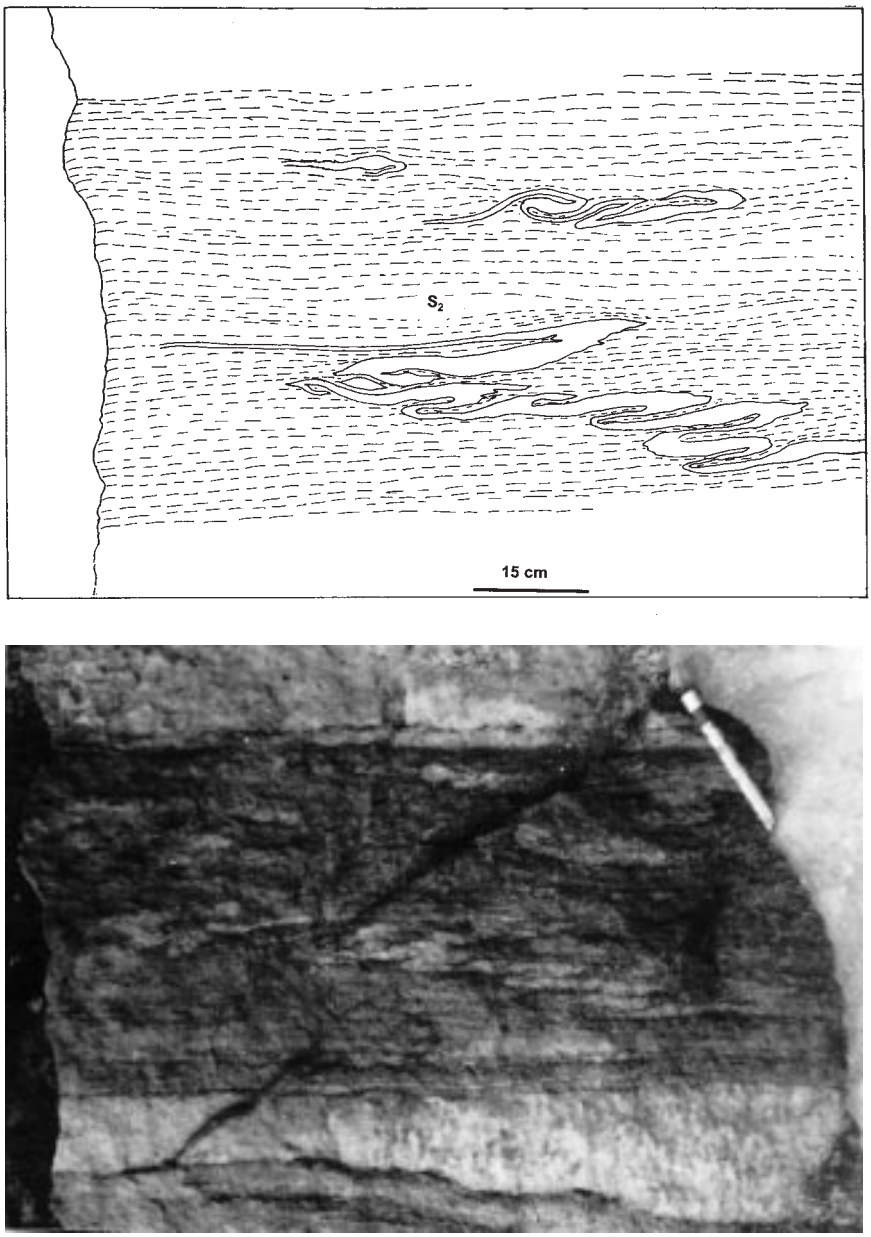

Fig. 6. Early generation leucosomes defining a set of appressed isoclinal (F_2) folds occurring between thick leucocratic regions parallel to the S_2 fabric.

inclusions. Rims show well-developed crystal faces and contain oriented inclusions that define a fabric aligned with the S_2 matrix fabric. The latter feature indicates post-S_2 growth (Fig. 16a). Clinopyroxene is preserved only locally in the higher structural levels, as porphyroblasts or as worm-like grains in contact with hornblende. Porphyroblastic clinopyroxene shows extensive retrogressive breakdown to actinolite. Ilmenite is the dominant opaque mineral in the metabasites, and occurs intergrown with amphibole. Hornblende shows retrogressive breakdown to actinolite.

MINERAL CHEMISTRY

Minerals were analysed with a JEOL JCXA-733 electron microprobe analyser at Kyushu University, Japan, using

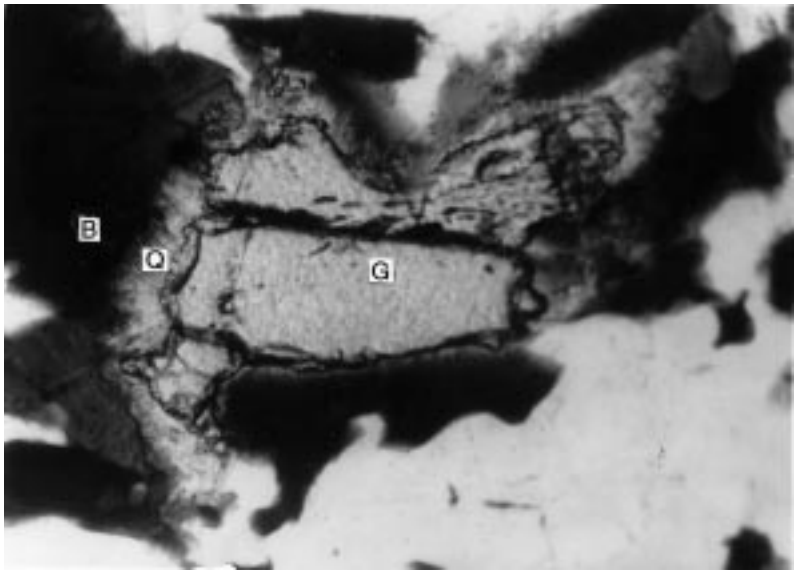

Fig. 7. Quartz (Q)–biotite (B) intergrowth replacing garnet (G) in pelitic rocks. Scale bar represents 125 μm.

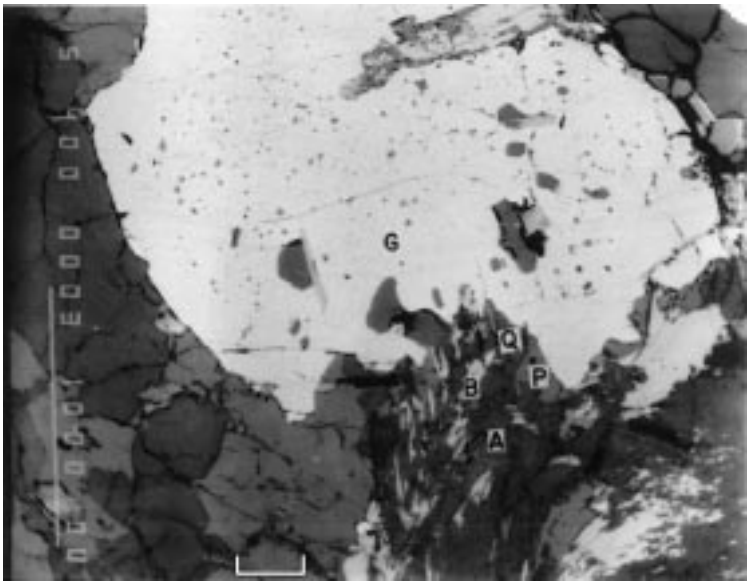

Fig. 8. Garnet (G) resorbed against an intergrowth of biotite (B), sillimanite (A), plagioclase (P) and quartz (Q) in pelitic migmatite. EPMA back-scatter image. Scale bar represents 250 μm.

an accelerating voltage of 15 kV and a beam current of 1×10^{-8} A. Natural mineral standards were used. A beam diameter of ~1 μm was used for most of the phases except scapolite, feldspars and calcite, where a broad beam (~10 μm) was used. JEOL ZAF software was used to correct the raw microprobe data. Representative mineral chemical data for the pelites, calc-silicate rocks, and metabasites are given in Tables 1, 2 and 3, respectively.

Pelitic rocks

In pelitic rocks, prograde and retrograde biotite can be distinguished by their TiO_2 contents. Retrograde biotite

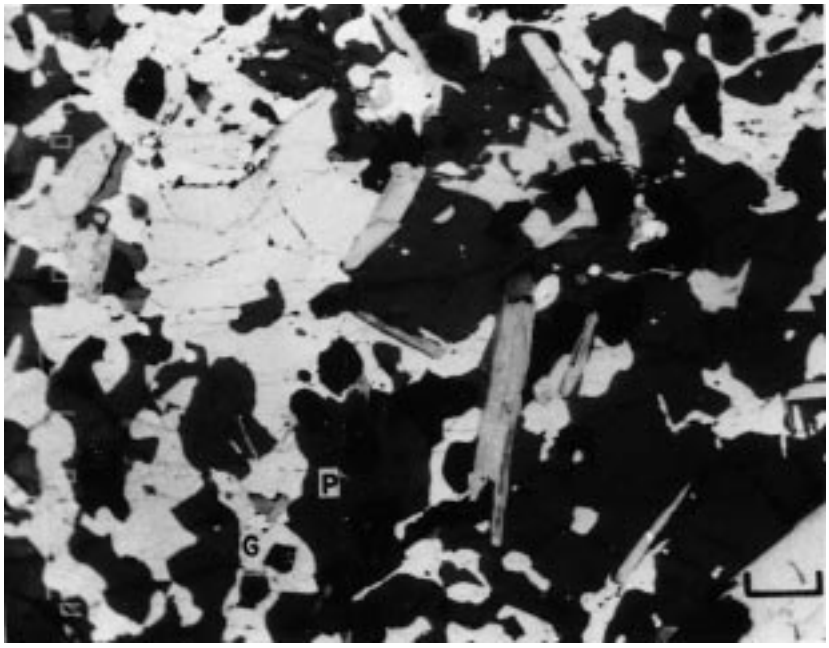

Fig. 9. Post-tectonic (S_2) skeletal garnet (G) overgrowing coarse matrix grains [plagioclase (P) and quartz] in pelitic migmatite. EPMA back-scatter image. Scale bar represents 250 μm.

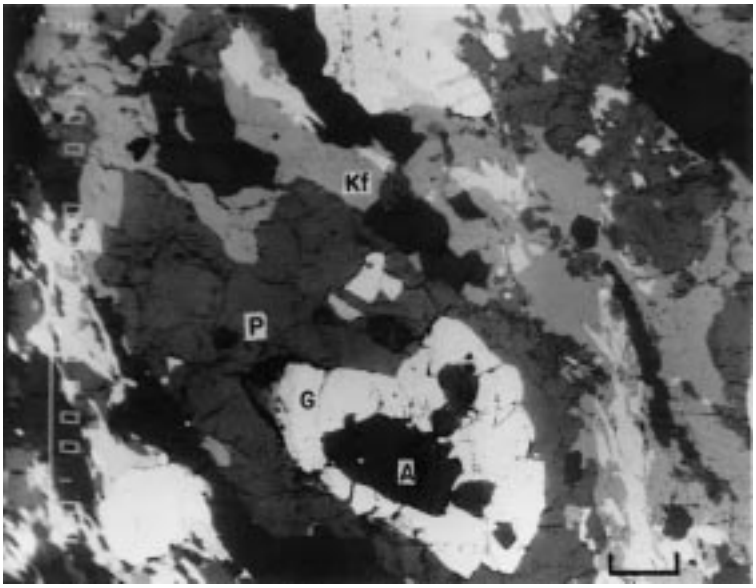

Fig. 10. Coronal garnet (G) rimming sillimanite (A) against plagioclase (P), bordering a leucosome vein in pelitic migmatite. Kf, K-feldspar. EPMA back-scatter image. Scale bar represents 250 μm.

grains show low TiO_2 (~0·4–0·6 wt %) compared with prograde ones (~2–4 wt %). Biotite compositions display very little variation within a given specimen. The maximum variation in X_{Mg} from core to rim in contact with garnet is ~0·05 (Analyses 29 and 28 in Table 1). Biotite grains in contact with garnet have X_{Mg} ~0·5 and TiO_2 0·6 wt %, whereas those in the matrix have X_{Mg} 0·19–0·45 and TiO_2 2–4 wt %. The higher X_{Mg} in the former grains may reflect diffusive re-equilibration during cooling. Locally, matrix biotite shows high Fe/Mg, a feature that may also have resulted from retrogression.

Garnet from pelitic rocks is $Alm_{60–65}Py_{20–30}Sp_{1–3}Gr_{7–20}$

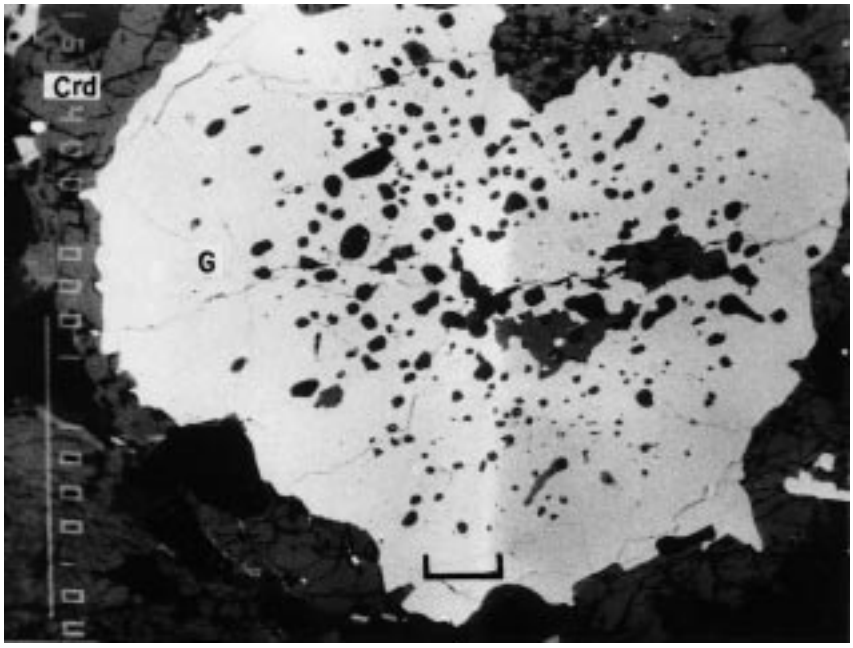

Fig. 11. Cordierite (Crd) rim on garnet (G) in pelitic rock. EPMA back-scatter image. Scale bar represents 250 μm.

(Table 1). Most garnet grains decrease in X_{Py} and increase in X_{Sp} from core to rim. Rimward depletion in X_{Py} and increase in X_{Alm} is observed in garnet grains adjacent to matrix biotite (Analyses 3 and 4, Table 1). These trends probably reflect post-peak garnet resorption and re-equilibration during cooling. X_{Gr} shows a sharp decrease near the rim in contact with plagioclase (Analyses 16 and 17, Table 1). Post-D_2 skeletal garnet is generally lower in X_{Gr} (0·13) compared with adjacent cores (X_{Gr} 0·2) (Analysis 15, Table 1). Garnet coronas between aluminosilicate minerals and plagioclase grains contain up to 9 mol % higher pyrope and lower almandine than the rims of other garnet grains in the same thin section (Analysis 5, Table 1). The low X_{Gr} of garnet rims and in texturally post-tectonic garnets suggests decompression.

Plagioclase in the pelitic rocks falls within the range $An_{55–37}Ab_{63–45}$ (Table 1) and contains maximum Or of ~4 mol %. Slightly larger plagioclase grains are unzoned except at their contacts with garnet. Such plagioclase rims display higher X_{An} (0·57) in comparison with the cores (0·49). Smaller plagioclase grains in contact with garnet are uniformly more calcic (X_{An} ~0·55) (Analysis 49, Table 1) than coarser grains. The small grains may have crystallized during the post-S_2 phase. Plagioclase inclusions within garnet always display higher anorthite contents than the matrix grains.

Spinel belongs to the $FeAl_2O_4$–$MgAl_2O_4$–$ZnAl_2O_4$ solid solution series with ~66 mol % hercynite and 10 mol % gahnite components. Spinel shows low Al ↔ Fe^{3+} substitution and contains low Ti. Cordierite is magnesian (X_{Mg} ~0·6) with negligible zoning.

Calc-silicate rocks

Porphyroblastic garnet from calc-silicate rocks contains 51–63 mol % grossular, with low andradite (~6–7 mol %) and pyrope (~2–4 mol %), and moderate almandine (29–34 mol %) (Table 2) contents. Grains lack significant zoning, except for minor rimward depletion of andradite near rims adjacent to clinopyroxene$_2$–plagioclase$_2$ symplectites. Hydrogrossular ($Gr_{79}And_{13}Py_8$) and wollastonite have been found in calc-silicate rocks next to a leucogranite body (sample Zemu, Analysis 67, Table 2).

Plagioclase compositions range between An_{38} and An_{75} (Table 2) . More calcic compositions (X_{An} 0·93) replace scapolite (EqAn 68) or occur with garnet. Some plagioclase grains are weakly zoned and display higher X_{An} at contacts with other Ca-bearing phases. Plagioclase$_2$ that occurs in symplectites with clinopyroxene$_2$ is highly calcic (X_{An} 0·95).

Clinopyroxene$_1$ occurs as a matrix mineral. It is diopside–hedenbergite$_{ss}$ with X_{Mg} = Mg/(Mg + Fe^{2+}) = 0·47–0·96 (Table 2) and contains little Al (Al_2O_3 0·17–0·35 wt %) in garnet-bearing samples. In garnet-free rocks, clinopyroxene may contain up to 3·17 wt % Al_2O_3 (Table 2). Clinopyroxene has low Fe^{3+} contents, calculated on the basis of charge balance criteria, and contains up to 13 mol % of CaTs. Clinopyroxene$_2$ occurs as symplectitic intergrowths with highly calcic plagioclase$_2$ (An_{96}). It has higher Al_2O_3 contents (2·6–3·5 wt %) and lower X_{Mg} (~0·4) than the clinopyroxene$_1$ matrix grains, and also shows significantly higher CaTs (16–17 mol %) and FeTs (8–10 mol %). Scapolite with EqAn ranging

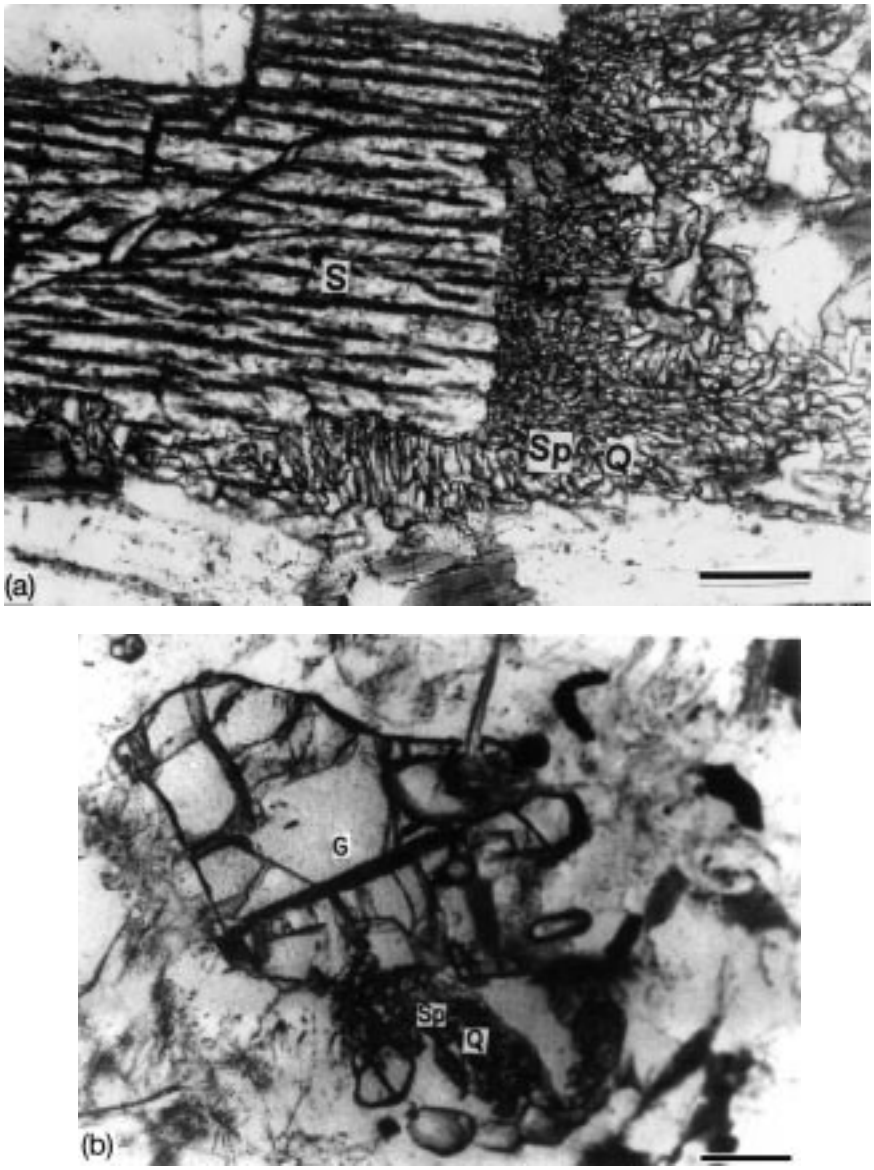

Fig. 12. (a) Spinel (Sp)–quartz (Q) intergrowth rimming sillimanite (S) in pelitic migmatite. Scale bar represents 50 μm. (b) Spinel (Sp)–quartz (Q) symplectite replacing garnet (G) in pelitic migmatite. Scale bar represents 125 μm.

from 65 to 70 (Table 2), contains negligible SO_3 and Cl. Pistacite contents of epidote vary from 0·17 to 0·25.

Metabasic rocks

Amphiboles span the compositional range of magnesiohornblende to tschermakitic hornblende, based on the 13 ex CNK scheme (Robinson *et al.*, 1982). They display low to moderate Ti (up to 1·45 wt % TiO_2, Table 3) contents. Ti correlates with the bulk X_{Mg} of the rock. Fe^{3+} (calculated from stoichiometry) ranges from 0·49 to 0·79. Secondary amphiboles that replace orthopyroxene are magnesiocummingtonite or anthophyllite with up to 38 mol % Fe.

Garnets in metabasic rocks display 50–65% almandine, 10–30% pyrope, 2–13% spessartine and relatively high proportion of grossular (16–25%) (Table 3). Grains are zoned and generally show trends of increasing X_{Py} and decreasing X_{Sp} from core to rim. Resorbed garnet grains surrounded by plagioclase (X_{An} ~0·85)–orthopyroxene symplectites display rimward decreases of X_{Gr} and X_{Py}, and an increase in X_{Sp}. Composite garnet grains exhibit complex zoning characteristics (Fig. 17a and b). The 'core' shows a slight rimward decrease in X_{Gr} and X_{Py}, whereas the outer rim displays increasing X_{Py} and

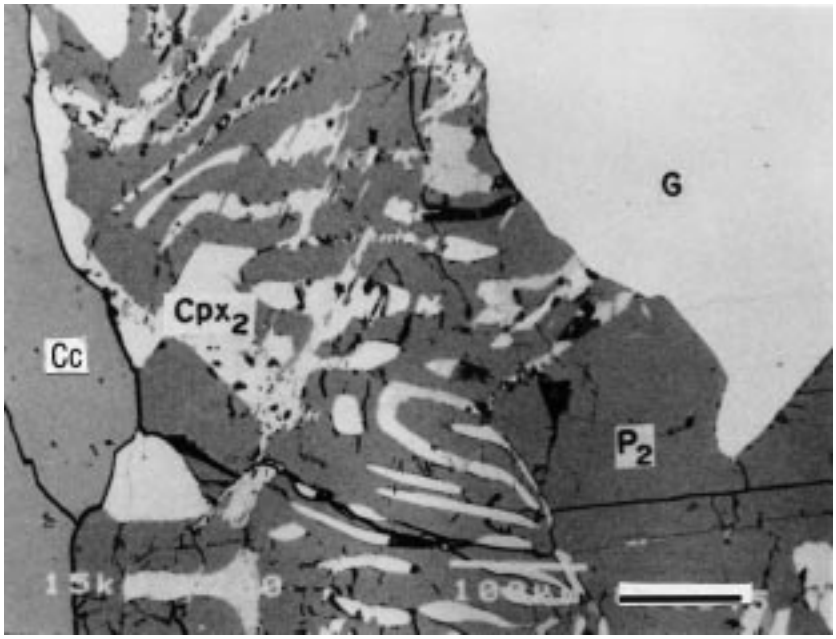

Fig. 13. Porphyroblastic garnet (G) rimmed by a symplectite of clinopyroxene (Cpx_2) and plagioclase (P_2) against calcite (Cc) in calc-silicate rock. EPMA back-scatter image. Scale bar represents 100 μm.

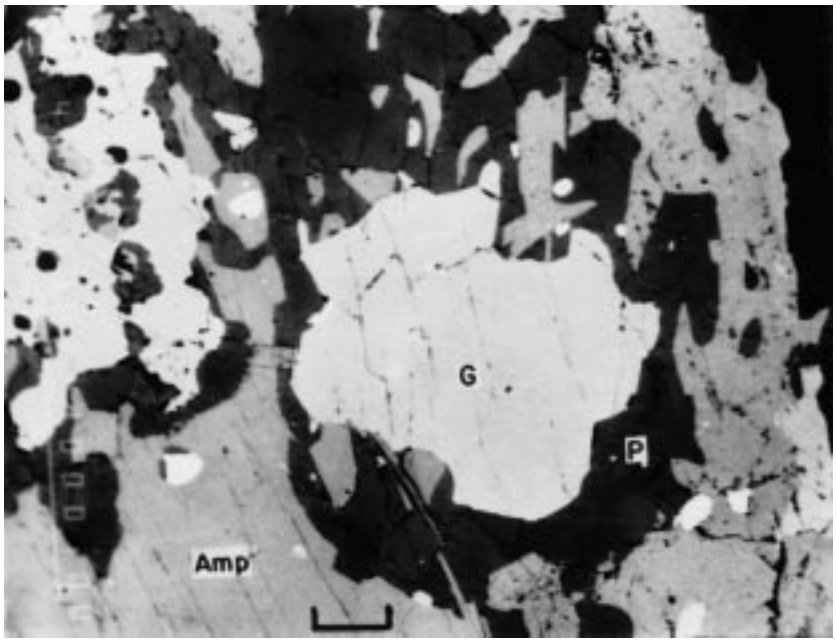

Fig. 14. Garnet (G) surrounded by a moat of plagioclase (P). Amp, amphibole. EPMA back-scatter image. Scale bar represents 250 μm.

decreasing X_{Sp} at almost constant X_{Gr}. The thin mantle of plagioclase that separates the two parts of composite garnet grains is highly calcic (X_{An} ~0·95) (Table 3). A zoning profile for composite grains in which the plagioclase mantle is incompletely developed or missing is shown in Fig. 17b.

Matrix plagioclase typically displays An_{40} compositions with low Or contents (Table 3). In contrast, plagioclase inclusions in garnet are anorthite rich. The increase in An content of plagioclase rims in contact with garnet grains appears to be related to the depletion of X_{Gr} in the rims of garnet. Clinopyroxene has X_{Mg} ~0·65–0·70.

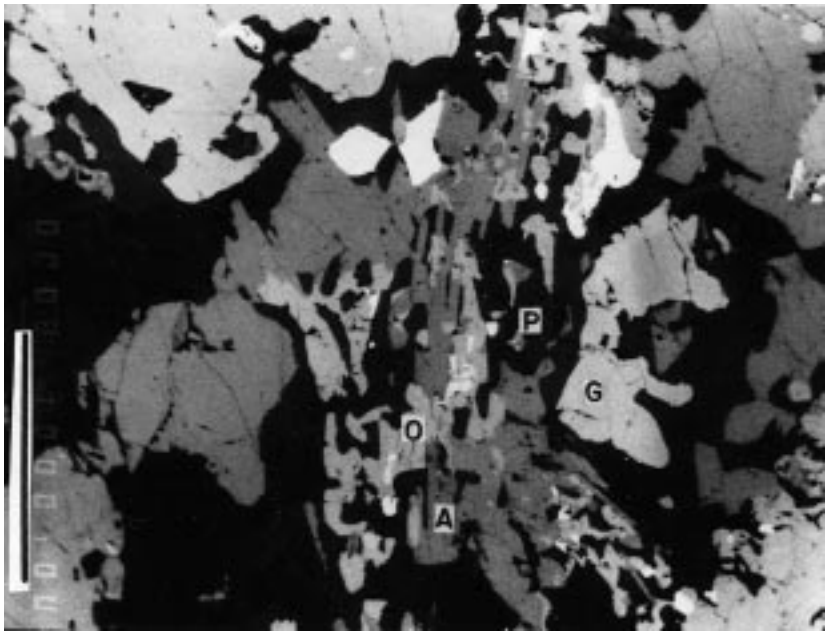

Fig. 15. Garnet (G) breaking down to a symplectite of orthopyroxene (O) and plagioclase (P). Orthopyroxene has subsequently broken down to amphibole (A). EPMA back-scatter image. Scale bar represents 250 μm.

Orthopyroxene has low X_{Al} (0·008) and X_{Mg} ~0·52 (Table 3). Ilmenite contains up to 2·65 wt % Fe_2O_3 and displays low Mn (2 mol %) and low Mg (<1 mol %) contents.

MINERAL REACTIONS AND EVOLUTION OF THE ASSEMBLAGES

Textures provide strong indications of the polymetamorphic history of these rocks. The cores of composite garnets showing two stages of growth are inferred to have grown before the D_2 deformation during an M_1 phase. This was followed by a dominant prograde metamorphic event (M_{2a}) during D_2, and lasted into the post-D_2 static period (M_{2b}). The most important prograde mineralogical change of the M_{2a} phase in the pelites is the elimination of primary muscovite, common in lower-grade rocks of Sikkim (Banerjee *et al.*, 1983; Mohan *et al.*, 1989). The elimination of muscovite in pelitic rocks can be attributed to either dehydration or melting reactions. Metamorphic pressures in the muscovite-bearing metapelites in the Sikkim region exceeded 4 kbar (see Mohan *et al.*, 1989), and it has been experimentally shown (e.g. Le Breton & Thompson, 1988; Vielzeuf & Holloway, 1988) that at pressures higher than 4 kbar melting is favoured over dehydration. We, therefore, argue that the elimination of muscovite during the M_{2a} event took place because of the incongruent melting reaction

$$\text{muscovite} + \text{plagioclase} + \text{quartz} = \text{biotite} + \text{sillimanite} + \text{K-feldspar} + L_1. \quad (1)$$

Melts generated by reaction (1) will be peraluminous, nearly water saturated and very small in amount (~1–4 %), largely proportional to the amount of muscovite available (Vielzeuf & Holloway, 1988). The small amount of melt will be unable to migrate from the site of generation (Vielzeuf & Holloway, 1988). We interpret the granitic leucosomes parallel to the S_2 fabric in the studied rocks to represent the *in situ* segregation of the melt produced through reaction (1).

Melting during metamorphism can occur either in fluid-present or in fluid-absent conditions (see Le Breton & Thompson, 1988; Vielzeuf & Holloway, 1988). Several lines of evidence suggest that melting of the Higher Himalayan Crystalline pile occurred under fluid-absent conditions. First, melting was mostly confined to 'fertile' lithologies, in contrast to more widespread melting that would be expected under fluid-present conditions (Clemens & Vielzeuf, 1987). Added to this are the constraints of limited porosity of rocks at mid- to lower-crustal levels, and the tendency of the fluids to be channelized. Furthermore, fluids would be immediately partitioned into melts. Trace element studies also argue against the presence of a pervasive fluid during metamorphism in the region (Harris *et al.*, 1993).

The bulk of mineral growth took place during the M_{2b} event, which coarsened matrix grains and produced post-tectonic grains as well as rims of garnet. Textural features,

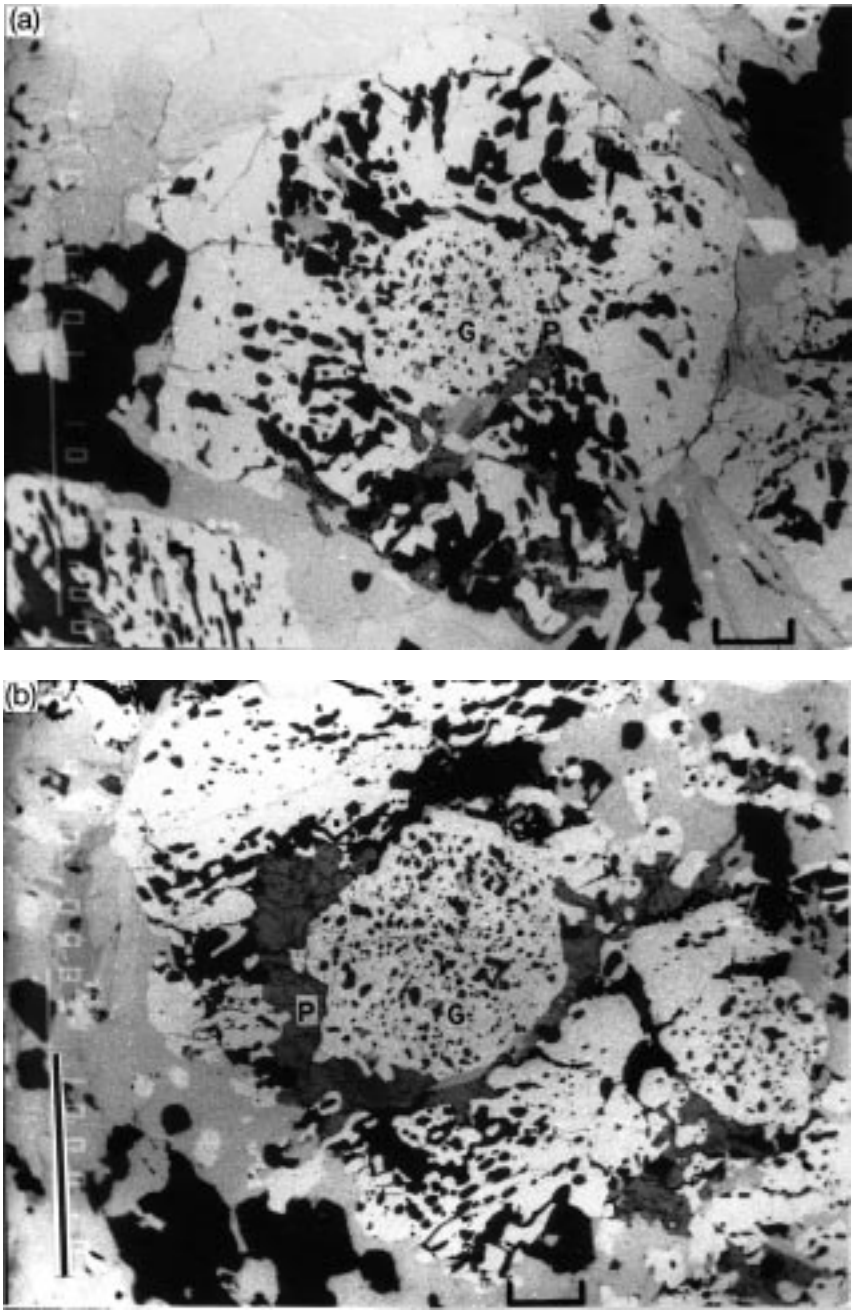

Fig. 16. (a) Composite garnet (G) grain with texturally distinct central part containing fine oriented inclusions of plagioclase and quartz and an outer part showing idiomorphic grain boundary and an internal fabric continuing into the external fabric at the bottom of the picture. A partly developed plagioclase (P) mantle separates the two parts. EPMA back-scatter image. Scale bar represents 250 μm. (b) Composite garnet (G) grain with a more completely developed plagioclase (P) mantle around the central part. EPMA back-scatter image. Scale bar represents 250 μm.

such as garnet separating sillimanite and plagioclase grains, the presence of garnet-bearing leucosomes, and the occurrence of veins and patchy leucosomes discordant to the metamorphic layering point to a second melting event involving the reaction

$$\text{biotite} + \text{sillimanite} + \text{plagioclase} + \text{quartz} = \text{garnet} + (\text{K-feldspar}) + L_2 \quad (2)$$

(Le Breton & Thompson, 1988; Vielzeuf & Holloway, 1988).

Table 1: Representative analyses from pelitic rocks

	Garnet										
Analysis:	1	2	3	4	5	6	7	8	9	10	11
Sample:	699/87/2-1 (C)	699/87/2-2 (R)	9/89/2-1/ (C)	9/89/2-2 (R)	9/89/1-3(Cor)	2/89/1-1 (C)	2/89/1-2 (R)	113/88/1-1 (C)	113/88/1-4 (R)	726/87/3-1 (C)	726/87/3-3 (R)
SiO_2	39·15	38·51	38·83	38·69	38·98	38·98	38·88	38·30	37·86	37·13	37·40
Al_2O_3	22·00	21·51	22·19	22·19	22·09	22·25	22·11	21·94	21·79	21·01	21·01
FeO	28·79	29·48	31·35	33·06	30·31	27·26	29·29	33·04	34·39	31·64	31·76
MgO	7·62	6·05	7·15	5·35	7·59	8·12	8·07	5·23	3·73	5·91	4·52
MnO	1·58	3·31	1·12	1·54	1·28	0·90	0·70	1·17	1·51	0·79	1·00
CaO	1·76	1·87	0·87	0·86	1·14	2·88	1·29	1·35	1·95	2·27	2·94
K_2O	0·00	0·03	0·02	0·03	0·00	0·01	0·00	0·00	0·00	0·01	0·00
Na_2O	0·04	0·01	0·01	0·00	0·02	0·00	0·00	0·01	0·02	0·00	0·04
TiO_2	0·04	0·04	0·00	0·01	0·02	0·03	0·04	0·06	0·02	0·04	0·04
Total	100·98	101·21	101·61	101·75	101·43	100·43	100·45	101·21	101·27	98·49	98·71
Cations (12 oxygen)											
Si	3·012	3·000	2·992	3·005	2·998	2·997	3·001	2·995	2·989	2·986	3·005
Al	1·995	1·975	2·015	2·031	2·002	2·016	2·011	2·022	2·028	1·991	1·990
Fe	1·853	1·920	2·020	2·147	1·949	1·753	1·891	2·161	2·271	2·128	2·134
Mg	0·874	0·703	0·821	0·619	0·870	0·931	0·929	0·610	0·439	0·622	0·541
Mn	0·103	0·218	0·073	0·101	0·083	0·059	0·046	0·078	0·101	0·052	0·068
Ca	0·145	0·156	0·072	0·072	0·094	0·237	0·107	0·113	0·165	0·196	0·253
K	0·000	0·003	0·002	0·003	0·000	0·001	0·000	0·000	0·000	0·001	0·000
Na	0·006	0·002	0·001	0·000	0·003	0·000	0·000	0·002	0·003	0·000	0·006
Ti	0·002	0·002	0·000	0·001	0·001	0·002	0·002	0·004	0·001	0·002	0·002
Total	7·990	8·002	8·000	7·980	8·000	7·996	7·991	7·991	7·997	8·004	7·999
X_{Mg}	0·29	0·23	0·27	0·21	0·29	0·31	0·31	0·21	0·15	0·21	0·18
X_{Fe}	0·62	0·64	0·68	0·73	0·65	0·59	0·64	0·73	0·76	0·71	0·71
X_{Ca}	0·05	0·05	0·02	0·02	0·03	0·08	0·04	0·04	0·05	0·06	0·08
X_{Mn}	0·03	0·07	0·02	0·03	0·03	0·02	0·02	0·03	0·03	0·02	0·02

	Garnet											
Analysis:	12	13	14	15	16	17	18	19	20	21	22	23
Sample:	115/88/2-1 (C)	115/88/2-2 (R)	14/89/1-4 (P)	14/89/1-1 (C)	20/89/A3-1 (C)	20/89/A3-2 (R)	64/86/1-1 (C)	64/86/1-3 (R)	64/86/3-4 (C)	64/86/3-5 (R)	108/88/2-1 (C)	108/88/2-2 (R)
SiO_2	38·80	38·06	37·99	37·94	39·12	38·85	39·62	39·27	39·32	39·10	38·94	38·14
Al_2O_3	21·77	21·50	20·70	20·56	22·00	21·97	21·97	22·05	21·79	21·81	21·59	21·46
FeO	32·86	33·96	28·19	26·79	27·09	30·87	27·80	30·96	27·80	30·53	31·66	33·58
MgO	4·91	3·12	2·37	2·57	6·61	6·99	7·63	7·14	7·21	7·22	5·57	3·62
MnO	1·35	2·72	6·53	4·45	1·94	1·49	0·77	0·95	0·95	0·98	1·23	2·39
CaO	1·64	1·16	4·62	7·10	4·27	1·25	2·95	1·10	3·09	1·67	2·04	1·90
K_2O	0·00	0·01	0·01	0·01	0·02	0·00	0·00	0·02	0·00	0·00	0·00	0·00
Na_2O	0·03	0·00	0·00	0·01	0·02	0·00	0·01	0·00	0·00	0·02	0·00	0·00
TiO_2	0·06	0·00	0·02	0·12	0·02	0·00	0·00	0·01	0·04	0·01	0·00	0·01
Total	101·60	100·64	100·53	100·36	101·37	101·58	100·76	101·50	100·24	101·34	101·04	101·12
Cations (12 oxygen)												
Si	3·023	3·028	3·033	3·014	3·007	2·997	3·037	3·019	3·037	3·013	3·033	3·015
Al	1·999	2·016	1·948	1·925	1·993	1·998	1·985	1·998	1·984	1·981	1·982	2·00
Fe	2·141	2·260	1·862	1·780	1·742	1·992	1·782	1·991	1·796	1·967	2·062	2·220
Mg	0·570	0·370	0·282	0·304	0·758	0·804	0·872	0·818	0·830	0·830	0·647	0·427
Mn	0·089	0·183	0·442	0·299	0·126	0·097	0·050	0·062	0·062	0·064	0·081	0·160
Ca	0·137	0·099	0·395	0·604	0·352	0·103	0·242	0·091	0·256	0·138	0·170	0·161
K	0·000	0·001	0·001	0·001	0·002	0·000	0·000	0·002	0·000	0·000	0·000	0·000
Na	0·005	0·000	0·000	0·002	0·003	0·000	0·001	0·000	0·000	0·003	0·000	0·000
Ti	0·004	0·000	0·001	0·007	0·001	0·000	0·000	0·001	0·002	0·001	0·000	0·001
Total	7·976	7·963	7·989	7·994	7·997	8·000	7·969	7·982	7·968	7·997	7·975	7·985
X_{Mg}	0·19	0·13	0·09	0·10	0·25	0·27	0·29	0·28	0·28	0·27	0·22	0·14
X_{Fe}	0·73	0·78	0·62	0·60	0·58	0·66	0·60	0·67	0·61	0·65	0·69	0·75
X_{Ca}	0·05	0·03	0·13	0·20	0·12	0·03	0·08	0·03	0·09	0·05	0·06	0·05
X_{Mn}	0·03	0·06	0·15	0·10	0·04	0·03	0·02	0·02	0·02	0·02	0·03	0·05

Table 1: continued

	Biotite									
Analysis:	24	25	26	27	28	29	30	31	32	33
Sample:	9/89/2-7(Con)	9/89/2-3	699/87/2-4(Con)	699/872-5 (M)	108/88/2-4(M)	108/88/2-3	108/88/2-8 (M)	2/89/3-5(Con)	113/88/3-3	726/87/3-8 (M)
SiO_2	36·39	36·54	35·45	35·96	36·38	35·61	35·87	36·37	35·97	35·31
Al_2O_3	18·57	17·94	19·10	17·87	20·15	18·82	18·95	20·35	18·59	17·53
FeO	16·53	16·49	18·82	19·71	17·32	18·73	19·08	15·02	19·39	19·33
MgO	12·04	11·37	9·74	10·35	10·11	8·59	9·10	12·46	9·63	9·21
MnO	0·03	0·10	0·14	0·07	0·20	0·15	0·25	0·07	0·03	0·07
CaO	0·00	0·00	0·04	0·00	0·00	0·00	0·00	0·04	0·00	0·03
K_2O	9·88	9·53	9·04	9·60	9·47	9·24	9·87	9·33	9·43	9·63
Na_2O	0·14	0·15	0·14	0·24	0·20	0·14	0·15	0·14	0·21	0·07
TiO_2	3·64	4·69	1·39	3·45	2·62	3·97	3·42	1·90	4·23	4·39
Total	97·22	96·81	93·86	97·25	96·45	95·25	96·69	95·68	97·48	95·57
Oxygen	10 (O)	+2 (OH)								
Si	2·679	2·697	2·722	2·685	2·698	2·698	2·691	2·685	2·673	2·686
Al	1·611	1·561	1·729	1·573	1·761	1·680	1·675	1·771	1·628	1·571
Fe	1·018	1·018	1·209	1·231	1·074	1·187	1·197	0·927	1·205	1·230
Mg	1·322	1·251	1·115	1·152	1·118	0·970	1·018	1·371	1·067	1·044
Mn	0·002	0·006	0·009	0·004	0·013	0·010	0·016	0·004	0·002	0·005
Ca	0·000	0·000	0·003	0·000	0·000	0·000	0·000	0·003	0·000	0·002
K	0·928	0·897	0·886	0·915	0·896	0·893	0·945	0·879	0·894	0·934
Na	0·020	0·021	0·021	0·035	0·029	0·021	0·022	0·020	0·030	0·010
Ti	0·202	1·561	0·080	0·194	0·146	0·226	0·193	0·106	0·236	0·251
Total	7·787	7·720	7·787	7·810	7·741	7·693	7·764	7·774	7·739	7·749
X_{Mg}	0·47	0·45	0·39	0·405	0·40	0·35	0·37	0·48	0·38	0·37
X_{Fe}	0·36	0·36	0·42	0·433	0·38	0·43	0·43	0·32	0·43	0·44
X_{Al}^{VI}	0·10	0·09	0·16	0·091	0·16	0·14	0·13	0·16	0·11	0·09
X_{Ti}	0·07	0·09	0·03	0·068	0·05	0·08	0·07	0·04	0·08	0·09

	Biotite				
Analysis:	34	35	36	37	38
Sample:	115/88/3-8	115/88/1-7	20/89/B3-2(Con)	20/89/B3-6(M)	64/86/2-4(Con)
SiO_2	35·53	35·80	37·25	36·99	37·36
Al_2O_3	20·03	19·42	18·26	17·60	19·39
FeO	19·40	18·86	14·93	15·39	17·24
MgO	8·48	8·20	13·28	13·07	11·55
MnO	0·05	0·07	0·07	0·00	0·07
CaO	0·01	0·00	0·00	0·00	0·00
K_2O	9·36	9·48	9·44	9·63	9·53
Na_2O	0·29	0·19	0·19	0·13	0·18
TiO_2	2·33	3·55	2·96	3·76	2·11
Total	95·48	95·57	96·38	96·57	97·43
Oxygen	10 (O)	+2 (OH)			
Si	2·692	2·702	2·734	2·722	2·737
Al	1·789	1·727	1·580	1·526	1·674
Fe	1·229	1·190	0·917	0·947	1·056
Mg	0·952	0·922	1·453	1·434	1·261
Mn	0·003	0·004	0·004	0·000	0·004
Ca	0·001	0·000	0·000	0·000	0·000
K	0·905	0·913	0·884	0·904	0·891
Na	0·043	0·028	0·027	0·019	0·026
Ti	0·133	0·202	0·163	0·208	0·116
Total	7·756	7·703	7·767	7·769	7·770
X_{Mg}	0·34	0·33	0·51	0·50	0·42
X_{Fe}	0·44	0·43	0·32	0·33	0·37
X_{Al}^{VI}	0·17	0·16	0·11	0·09	0·14
X_{Ti}	0·05	0·07	0·06	0·07	0·04

Table 1: continued

	Plagioclase										
Analysis:	39	40	41	42	43	44	45	46	47	48	49
Sample:	9/89/2-5	699/87/2-7	108/88/2-7	2/89/1-9	2/89/3-7	2/89/3-9	113/88/1-7	113/88/2-6	113/88/2-7	726/87/1-5 (R)	726/87/1-8
SiO_2	62·32	60·89	58·73	60·21	60·54	60·42	61·51	61·26	63·16	52·87	54·69
Al_2O_3	23·91	24·37	25·69	25·06	24·84	24·64	23·93	23·71	24·07	28·41	27·79
FeO	0·00	0·00	0·00	0·00	0·00	0·00	0·00	0·00	0·00	0·21	0·00
MgO	0·01	0·00	0·00	0·01	0·00	0·01	0·00	0·00	0·00	0·01	0·01
MnO	0·00	0·00	0·00	0·00	0·00	0·00	0·00	0·00	0·00	0·00	0·00
CaO	5·28	5·85	7·85	6·80	6·22	6·48	4·98	4·91	4·83	11·86	11·22
K_2O	0·25	0·14	0·14	0·18	0·31	0·28	0·16	0·34	0·16	0·14	0·14
Na_2O	7·57	7·72	6·61	7·10	7·24	7·09	7·74	7·69	8·11	4·66	4·96
TiO_2	0·01	0·00	0·00	0·00	0·05	0·01	0·00	0·00	0·00	0·04	0·05
Cr_2O_3											
Total	99·62	99·17	99·36	99·43	99·41	99·13	98·74	98·11	100·33	98·34	99·16
Cations (8 Oxygen)											
Si	2·766	2·724	2·638	2·690	2·704	2·707	2·753	2·761	2·776	2·435	2·489
Al	1·251	1·285	1·360	1·319	1·308	1·300	1·262	1·259	1·247	1·542	1·490
Fe	0·000	0·000	0·000	0·000	0·000	0·000	0·000	0·000	0·000	0·007	0·000
Mg	0·001	0·000	0·000	0·001	0·000	0·001	0··000	0·000	0·000	0·001	0·001
Mn	0·000	0·000	0·000	0·000	0·000	0·000	0·000	0·000	0·000	0·000	0·000
Ca	0·251	0·280	0·378	0·325	0·298	0·311	0·239	0·237	0·227	0·585	0·547
K	0·014	0·008	0·008	0·010	0·018	0·016	0·009	0·020	0·009	0·008	0·008
Na	0·651	0·670	0·576	0·615	0·627	0·616	0·672	0·672	0·691	0·416	0·438
Ti	0·000	0·000	0·000	0·000	0·002	0·000	0·000	0·000	0·000	0·001	0·000
Total	4·941	4·972	4·971	4·962	4·964	4·957	4·949	4·953	4·950	4·999	4·984
X_{An}	0·27	0·29	0·39	0·34	0·32	0·33	0·26	0·25	0·24	0·58	0·55

	Plagioclase				Cord	Spinel
Analysis:	50	51	52	53	54	55
Sample:	726/87/1-3 (C)	115/88/1-3	20/89/B3-4	20/89/A3-9	113/88/2-3	20/89/A/1-9
SiO_2	56·10	59·84	60·72	59·42	48·16	0·00
Al_2O_3	26·83	25·17	24·38	25·61	32·58	60·66
Fe_2O_3	—	—	—	—	—	0·80
FeO	0·00	0·00	0·00	0·00	9·58	28·15
MgO	0·01	0·00	0·00	0·00	7·61	5·81
MnO	0·00	0·00	0·00	0·00	0·21	0·16
CaO	9·71	6·66	6·30	7·83	0·02	0·00
K_2O	0·23	0·27	0·29	0·29	0·01	0·04
Na_2O	5·42	7·00	7·38	5·84	0·15	0·14
TiO_2	0·02	0·02	0·00	0·07	0·00	0·04
ZnO	—	—	—	—	—	4·67
Total	98·54	99·24	99·37	99·31	98·39	100·47
Oxygen	8	8	8	8	18	4
Si	2·555	2·681	2·715	2·660	4·991	0·000
Al	1·440	1·329	1·285	1·351	3·980	1·984
Fe^{3+}	—	—	—	—	—	0·017
Fe^{2+}	0·000	0·000	0·000	0·000	0·830	0·653
Mg	0·001	0·000	0·000	0·000	1·176	0·240
Mn	0·000	0·000	0·000	0·000	0·018	0·004
Ca	0·474	0·320	0·302	0·376	0·002	0·000
Zn	—	—	—	—	—	0·096
K	0·013	0·015	0·017	0·017	0·001	0·001
Na	0·479	0·608	0·640	0·507	0·030	0·008
Ti	0·001	0·001	0·000	0·002	0·000	0·001
Total	4·970	4·963	4·969	4·920	11·033	3·004
X_{An}	0·49	0·339	0·315	0·418	—	—
X_{Mg}	—	—	—	—	0·59	0·27

C, core composition; R, rim composition; Cor, coronal garnet; P, post-tectonic (D_2) garnet; Con, grains in contact with garnet; M, matrix grains (samples in biotite section without connotation are grains near garnet but not in contact); C, core of grain in contact with garnet. Analysis 29 is core and Analysis 28 is rim of biotite grain in contact with garnet. Analysis 49 is rim in contact with garnet.

Table 2: Representative chemical analyses from calc-silicate rocks

	Scapolite				Clinopyroxene				
Analysis:	56	57	58	59	60	61	62	63	64
Sample:	103/88 1-13	N/24 2-4	N/24 3-2	N/15 2-11	103/88 2-2	Zemu 1-1	N/24 1-1	107/88 1-1	54/94/ 1-3
SiO_2	44·43	46·08	45·93	45·46	51·63	53·24	55·08	51·32	47·38
Al_2O_3	28·10	27·51	27·53	28·08	0·60	0·33	1·12	0·93	3·41
FeO	0·00	0·00	0·00	0·00	16·46	9·17	2·32	15·73	17·07
MgO	0·03	0·04	0·04	0·03	8·02	12·27	17·17	8·38	6·18
MnO	0·00	0·03	0·00	0·00	0·61	0·13	0·01	0·46	0·65
CaO	19·74	18·83	18·85	19·27	23·43	25·41	25·59	23·20	23·52
K_2O	0·06	0·03	0·13	0·14	0·00	0·00	0·00	0·03	0·00
Na_2O	2·42	3·02	2·79	2·54	0·23	0·12	0·30	0·13	0·21
TiO_2	0·03	0·00	0·00	0·01	0·06	0·00	0·02	0·15	0·32
SO_3	0·00	0·00	0·01						
Cl	0·05	0·04	0·02						
Total	95·04	95·65	95·45	95·72	101·25	100·88	101·73	100·38	98·74
Oxygen	25	25	25	25	6	6	6	6	6
Si	6·979	7·162	7·152	7·069	1·984	1·989	1·973	1·979	1·871
Al	5·202	5·039	5·052	5·146	0·027	0·015	0·047	0·042	0·160
Fe^{3+}	—	—	—	—	0·021	0·019	0·037	0·002	0·096
Fe^{2+}	0·014	0·005	0·013	0·015	0·507	0·267	0·032	0·506	0·468
Mg	0·007	0·009	0·009	0·007	0·459	0·683	0·917	0·482	0·364
Mn	—	0·004	—	—	0·020	0·004	0·000	0·015	0·022
Ca	3·322	3·135	3·145	3·211	0·965	1·017	0·982	0·959	0·995
K	0·012	0·006	0·026	0·028	0·000	0·000	0·000	0·001	0·000
Na	0·737	0·910	0·842	0·766	0·017	0·009	0·021	0·010	0·016
Ti	0·004	—	—	0·001	0·002	0·000	0·001	0·004	0·010
S^{6+}	—	—	0·001	·0013					
Cl	0·013	0·011	0·005						
Total	16·284	16·275	16·247	16·246	4·008	4·008	4·013	4·000	4·032
EqAn	70·8	65·2	65·6	68·5	—	—	—	—	—
Di	—	—	—	—	95·0	97·5	94·9	95·6	74·0
CaTs	—	—	—	—	2·8	1·07	3·2	4·16	16·17
FeTs	—	—	—	—	2·2	1·36	1·9	0·19	9·76
X_{Mg}	—	—	—	—	0·47	0·71	0·96	0·48	0·43

	Wollastonite		Garnet				Amphibole		
Analysis:	65	66	67	68	69	70	71	72	73
Sample:	Zemu 2-3	Zemu 2-9	Zemu 2-2	54/94/ 1-1	54/94/ 3-1 (C)	54/94/ 3-5 (R)	103/88 1-10	N/24 1-2	107/88 2-2
SiO_2	51·74	51·63	37·11	38·08	37·82	38·25	42·99	56·81	54·09
Al_2O_3	0·01	0·00	17·89	20·11	20·42	20·55	10·79	1·32	0·91
Fe_2O_3	—	—	3·82	2·71	2·36	2·10	—	—	—
FeO	0·43	0·27	0·00	14·10	15·50	15·68	23·11	3·09	15·75
MgO	0·04	0·05	1·98	0·74	1·22	1·18	6·76	22·47	13·90
MnO	0·09	0·00	0·00	2·54	1·73	1·63	0·46	0·00	0·12
CaO	48·26	48·39	36·47	21·75	20·54	20·77	12·21	13·78	12·57
K_2O	0·00	0·00	0·03	0·00	0·00	0·00	0·58	0·15	0·05
Na_2O	0·00	0·00	0·04	0·01	0·00	0·01	1·07	0·21	0·06
TiO_2	0·00	0·00	0·12	0·10	0·12	0·14	0·14	0·05	0·04
Total	100·71	100·40	97·53	100·14	99·71	100·31	98·11	97·88	97·49
Oxygen	6	6	12	12	12	12	*	*	*
Si	1·992	1·993	2·920	2·981	2·969	2·892	6·528	7·816	7·885
Al	0·000	0·000	1·659	1·856	1·890	1·888	1·954	0·214	0·157
Fe^{3+}			0·230	0·159	0·139	0·123	0·579	0·000	0·113
Fe^{2+}	0·014	0·000	0·000	0·923	1·018	1·022	2·355	0·356	1·807
Mg	0·002	0·003	0·232	0·086	0·143	0·137	1·530	4·609	3·020
Mn	0·003	0·000	0·000	0·168	0·115	0·108	0·060	0·000	0·015
Ca	1·991	2·001	3·075	1·825	1·728	1·735	1·987	2·031	1·963
K	0·000	0·000	0·003	0·000	0·000	0·000	0·112	0·026	0·009
Na	0·000	0·000	0·006	0·002	0·000	0·002	0·315	0·056	0·017
Ti	0·000	0·000	0·007	0·006	0·007	0·008	0·016	0·005	0·004
Total	4·006	4·008	8·132	8·006	8·009	8·005	15·414	15·114	14·990
Py	—	—	8·19	2·76	4·70	4·54	—	—	—
Alm	—	—	—	29·71	33·44	33·88	—	—	—
Gr	—	—	79·63	51·73	51·24	51·88	—	—	—
And	—	—	12·17	7·67	6·85	6·11	—	—	—
X_{Mg}	—	—	—	—	—	—	0·39	0·93	0·62

Table 2: continued

	Plagioclase					Titanite
Analysis:	74	75	76	77	78	79
Sample:	103/88 1-4	103/88 1-5	N/24 3-8	54/94/ 1-5	107/88 1-4	107/88 2-8
SiO_2	59·18	51·55	58·43	43·44	43·55	30·22
Al_2O_3	25·48	31·08	25·85	35·79	35·12	2·86
FeO	0·00	0·00	0·00	0·28	0·00	0·00
MgO	0·00	0·00	0·01	0·01	0·00	0·03
MnO	0·00	0·00	0·00	0·00	0·00	0·00
CaO	7·75	14·35	8·20	19·97	19·40	29·12
K_2O	0·14	0·06	0·46	0·00	0·04	0·03
Na_2O	7·03	3·57	6·57	0·37	0·31	0·03
TiO_2	0·00	0·05	0·00	0·00	0·00	35·46
Total	99·62	100·70	99·64	99·86	98·67	98·27
Si	2·650	2·329	2·624	2·018	2·043	1·003
Al	1·345	1·655	1·368	1·959	1·941	0·112
Fe	0·000	0·000	0·000	0·010	0·000	0·000
Mg	0·000	0·000	0·001	0·001	0·000	0·001
Mn	0·000	0·000	0·000	0·000	0·000	0·000
Ca	0·372	0·695	0·395	0·994	0·975	1·035
K	0·008	0·003	0·026	0·000	0·002	0·001
Na	0·610	0·313	0·572	0·033	0·028	0·002
Ti	0·000	0·002	0·000	0·000	0·000	0·885
Total	4·986	4·998	4·990	5·015	4·998	3·052
X_{An}	0·37	0·69	0·40	0·97	0·97	—

Fe^{3+} from stoichiometry, except $*Fe^{3+}$ in amphibole from charge balance criteria according to the 13 e CNK scheme (Robinson *et al.*, 1982). EqAn = [(Al − 3)/3] × 100, calculated on the basis of Si + Al normalized to 12 cations. Di = I/[Mg + (Al/2) + (Fe^{3+}/2)], where I = Mg, Al/2, Fe^{3+}. X_{Mg} = Mg/(Mg + Fe^{2+}). Samples 107/88 and 54/94 are from the same outcrop. Analysis 63 is matrix clinopyroxene. Analysis 64 is $clinopyroxene_2$ in calc-silicate. Analysis 67 is hydrogrossular. Analysis 72 is tremolite replacing matrix clinopyroxene. Analysis 77 is $plagioclase_2$ forming symplectite with $clinopyroxene_2$.

Table 3: Representative chemical analyses from metabasic rocks

	Garnet								
Analysis:	80	81	82	83	84	85	86	87	88
Sample:	642/87 3-1	642/87 3-2	642/87 3-4	665/87 1-6	690/87/2-1 (C)	690/87/2-2 (R)	97/88 2-1	88/88 1-1 (C)	88/88 1-4 (R)
SiO_2	37·71	37·93	38·68	37·91	39·16	39·37	38·91	38·75	39·08
Al_2O_3	20·88	20·89	21·68	21·35	21·98	21·75	21·74	21·93	21·89
FeO	23·14	25·25	24·96	29·42	23·61	23·23	27·72	25·38	24·87
MgO	2·76	2·30	3·18	2·34	6·63	5·40	3·99	3·52	5·89
MnO	5·99	3·88	2·30	3·55	1·51	2·10	1·15	4·13	2·03
CaO	9·80	9·34	9·55	5·92	7·52	9·10	7·89	7·93	7·13
K_2O	0·03	0·02	0·00	0·00	0·00	0·00	0·01	0·01	0·00
Na_2O	0·06	0·07	0·07	0·02	0·00	0·00	0·00	0·00	0·02
TiO_2	0·08	0·08	0·04	0·07	0·00	0·09	0·07	0·05	0·03
Total	100·51	100·40	100·51	100·58	100·57	101·09	101·52	101·80	101·29
Si	2·978	3·004	3·021	3·010	3·008	3·021	3·013	3·003	3·003
Al	1·943	1·950	1·996	1·998	1·990	1·967	1·984	2·003	1·983
Fe	1·520	1·673	1·630	1·954	1·516	1·491	1·795	1·645	1·598
Mg	0·325	0·272	0·370	0·277	0·759	0·618	0·461	0·407	0·675
Mn	0·401	0·260	0·152	0·239	0·098	0·137	0·075	0·271	0·132
Ca	0·829	0·793	0·799	0·504	0·619	0·748	0·655	0·658	0·587
K	0·003	0·002	0·000	0·000	0·000	0·000	0·001	0·001	0·000
Na	0·009	0·011	0·011	0·003	0·000	0·000	0·000	0·000	0·003
Ti	0·005	0·005	0·002	0·004	0·000	0·005	0·004	0·003	0·002
Total	8·015	8·008	7·984	7·989	7·997	7·990	7·990	7·995	8·001
X_{Mg}	0·10	0·09	0·12	0·09	0·25	0·21	0·15	0·14	0·22
X_{Fe}	0·49	0·56	0·55	0·66	0·51	0·50	0·60	0·55	0·53
X_{Ca}	0·27	0·26	0·27	0·17	0·21	0·25	0·22	0·22	0·20
X_{Mn}	0·13	0·09	0·05	0·08	0·03	0·04	0·02	0·09	0·04

Table 3: continued

	Clinopyroxene		Amphibole						
Analysis:	89	90	91	92	93	94	95	96	97
Sample:	30/93/ 1-1	30/93/ 3-3	690/87 1-6	690/87 2-6	690/87 2-10	97/88 3-9	88/88 3-8	120/86 2-6	210/86 1-4
SiO_2	52·55	51·33	54·66	54·91	44·08	44·60	47·39	50·68	43·18
Al_2O_3	0·80	1·06	0·77	0·66	11·45	13·80	9·15	6·21	12·25
FeO	10·99	10·54	23·70	22·32	14·25	16·79	11·54	12·52	17·51
MgO	11·47	11·71	17·37	18·72	11·63	8·68	14·41	14·93	9·08
MnO	0·57	0·51	0·83	0·72	0·30	0·26	0·21	0·41	0·33
CaO	23·00	23·38	0·84	0·64	10·73	11·10	11·30	12·34	11·38
K_2O	0·02	0·00	0·00	0·01	0·81	0·30	0·57	0·53	1·01
Na_2O	0·34	0·36	0·07	0·06	1·54	1·20	0·71	0·75	0·95
TiO_2	0·12	0·13	0·08	0·08	2·06	0·41	1·91	0·35	1·46
Total	99·86	99·02	98·32	98·12	96·85	97·14	97·19	98·72	97·15
Oxygen	6	6	*						
Si	1·990	1·953	6·964	6·935	6·465	6·560	6·776	7·213	6·439
Al	0·036	0·048	0·116	0·098	1·981	2·394	1·543	1·034	2·154
Fe^{3+}	0·005	0·065	1·605	2·358	0·673	0·498	0·732	0·389	0·537
Fe^{2+}	0·342	0·270	0·000	0·000	1·075	1·568	0·648	1·102	1·646
Mg	0·647	0·664	3·298	3·524	2·542	1·903	3·071	3·167	2·018
Mn	0·018	0·016	0·090	0·077	0·037	0·032	0·025	0·049	0·042
Ca	0·933	0·953	0·115	0·087	1·686	1·749	1·731	1·882	1·818
K	0·001	0·000	0·000	0·002	0·152	0·057	0·104	0·096	0·192
Na	0·025	0·027	0·017	0·015	0·438	0·343	0·197	0·207	0·275
Ti	0·003	0·004	0·008	0·008	0·227	0·046	0·205	0·037	0·164
Total	4·001	4·000	13·132	13·103	15·276	15·148	15·032	15·185	15·285
X_{Mg}	0·65	0·71			0·71	0·55	0·82	0·86	0·55
Di	96·9	92·1			—	—	—	—	—

	Plagioclase								
Analysis:	98	99	100	101	102	103	104	105	106
Sample:	120/86 1-1	690/87/ 1-3	690/87 3-11	97/88 2-3	97/88 3-5	88/88 1-9	88/88 3-1	642/87 3-3	665/87 1-7
SiO_2	59·43	49·42	56·31	48·33	59·05	46·95	54·18	43·70	60·31
Al_2O_3	25·57	32·31	27·51	33·15	26·15	33·62	28·86	34·89	24·86
FeO	0·00	0·24	0·00	0·00	0·00	0·00	0·00	0·00	0·00
MgO	0·02	0·00	0·01	0·00	0·00	0·00	0·00	0·00	0·00
MnO	0·00	0·02	0·00	0·00	0·00	0·00	0·00	0·00	0·00
CaO	7·57	15·55	10·08	16·66	7·96	17·68	11·73	19·38	6·54
K_2O	0·46	0·04	0·12	0·01	0·09	0·01	0·08	0·02	0·07
Na_2O	6·12	2·60	5·64	1·97	6·99	1·57	3·87	0·51	7·35
TiO_2	0·00	0·00	0·00	0·00	0·04	0·00	0·00	0·00	0·00
Total	99·34	100·18	99·78	100·31	100·66	100·09	98·82	98·66	99·55
Oxygen	8	8	8	8	8	8	8	8	8
Si	2·662	2·253	2·535	2·206	2·622	2·157	2·465	2·050	2·693
Al	1·350	1·736	1·459	1·784	1·368	1·821	1·547	1·929	1·308
Fe	0·000	0·008	0·000	0·000	0·000	0·000	0·000	0·000	0·000
Mg	0·001	0·000	0·001	0·000	0·000	0·000	0·000	0·000	0·000
Mn	0·000	0·001	0·000	0·000	0·000	0·000	0·000	0·000	0·000
Ca	0·363	0·760	0·486	0·815	0·379	0·870	0·572	0·974	0·313
K	0·026	0·002	0·007	0·001	0·005	0·001	0·005	0·001	0·004
Na	0·531	0·230	0·492	0·174	0·602	0·140	0·341	0·046	0·636
Ti	0·000	0·000	0·000	0·000	0·001	0·000	0·000	0·000	0·000
Total	4·938	4·990	4·984	4·987	4·990	4·998	4·933	5·006	4·967
X_{An}	0·39	0·77	0·49	0·82	0·38	0·86	0·62	0·95	0·33

Table 3: continued

	Orthopyroxene			Rutile	Ilmenite			Magnetite
Analysis:	107	108	109	110	111	112	113	114
Sample:	690/87/ 1-8	690/87 2-11	690/87 3-10	88/88 1-2	97/88 3-11	88/88 2-8	665/87 1-2	665/87 3-1
SiO_2	52·20	52·02	52·58	0·00	0·00	0·02	0·02	0·05
Al_2O_3	0·90	1·12	0·82	0·05	0·00	0·03	0·02	0·51
Fe_2O_3					0·00	0·40	4·59	68·03
FeO	28·16	26·82	26·12	0·53	45·86	45·67	43·16	32·17
MgO	18·41	18·86	19·43	0·00	0·04	0·17	0·09	0·02
MnO	1·04	0·96	1·09	0·06	1·23	1·45	1·85	0·11
CaO	0·63	0·53	0·42	0·02	0·00	0·00	0·00	0·00
K_2O	0·00	0·00	0·00	0·00	0·00	0·00	0·02	0·00
Na_2O	0·03	0·00	0·01	0·01	0·00	0·02	0·02	0·00
TiO_2	0·10	0·15	0·12	99·37	53·83	52·72	50·26	0·69
Total	101·47	100·59	100·59	100·04	100·96	100·46	100·03	101·59
Oxygen	6	6	6	2	12	12	12	4
Si	1·973	1·973	1·984	0·000	0·000	0·002	0·002	0·002
Al	0·040	0·050	0·036	0·005	0·000	0·004	0·002	0·023
Fe^{3+}					0·000	0·300	0·345	1·934
Fe^{2+}	0·890	0·851	0·824	0·035	3·821	3·834	3·649	1·017
Mg	1·037	1·066	1·093	0·000	0·006	0·025	0·014	0·001
Mn	0·033	0·031	0·035	0·004	0·104	0·123	0·158	0·004
Ca	0·026	0·022	0·017	0·002	0·000	0·000	0·000	0·000
K	0·000	0·000	0·000	0·000	0·000	0·000	0·003	0·000
Na	0·002	0·000	0·001	0·002	0·000	0·000	0·004	0·000
Ti	0·003	0·004	0·003	5·975	4·034	3·981	3·822	0·020
Total	4·004	3·999	3·993	6·023	7·965	7·999	8·003	3·001
X_{Mg}	0·54	0·56	0·57	—	—	—	—	—
X_{Fe}	0·46	0·44	0·43	—	—	—	—	—
X_{FeTiO_2}	—	—	—	—	—	0·93	0·92	—

Fe^{3+} from charge balance criteria; $X_{Mg} = Mg/(Mg + Fe^{2+})$. Analyses 80 and 81 are core and rim, respectively, of central part of composite garnet grains. Analysis 82 represents the rim part of the composite garnet. Analysis 85 is rim of garnet rimmed by orthopyroxene–plagioclase symplectite. Analyses 89 and 90 are matrix clinopyroxene. Analyses 91 and 92 are anthophyllite replacing orthopyroxene. Analysis 99 is $plagioclase_2$ forming symplectites with orthopyroxene. Analysis 105 is plagioclase moat mantling central part of composite garnet. Analysis 107 is symplectitic orthopyroxene around garnet.
*Amphibole calculation according to the 13 e CNK scheme (Robinson *et al.*, 1982).

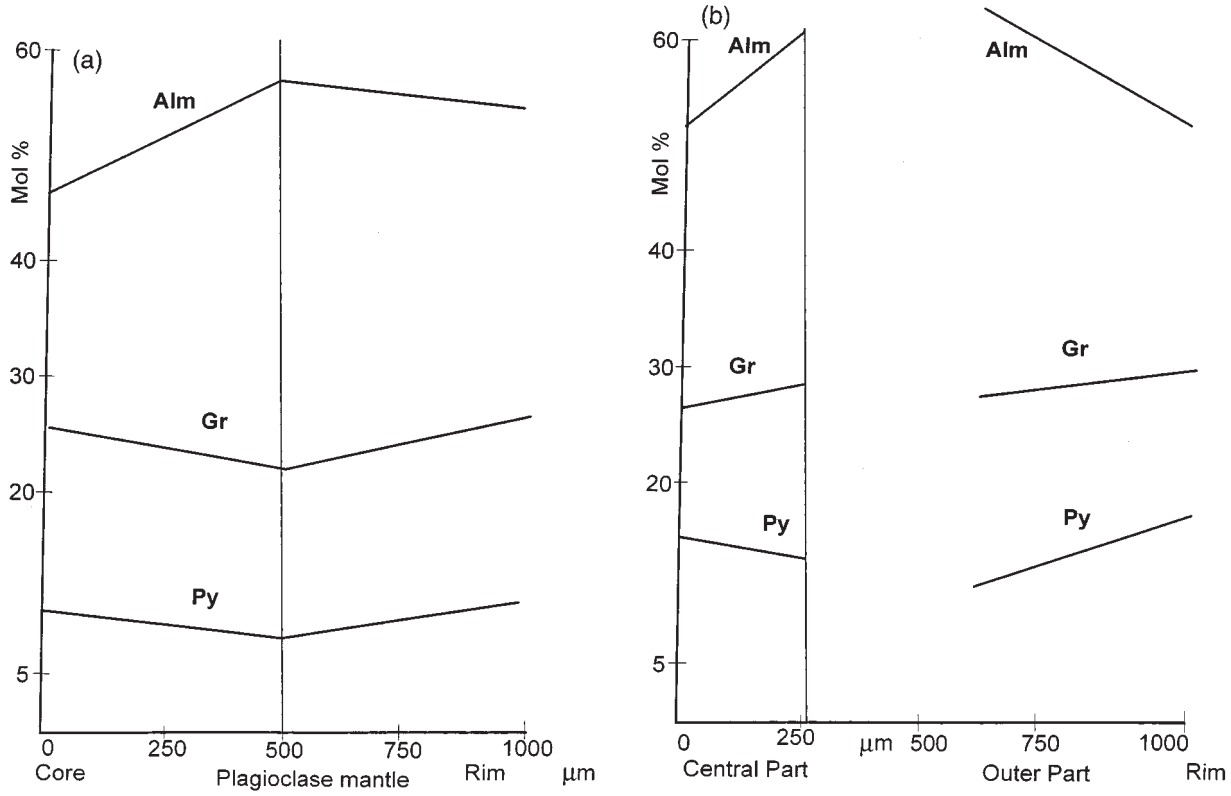

Fig. 17. Zoning profiles for composite garnet grains in metabasic rock. (a) Pattern where plagioclase mantle in the central part is well developed. (b) Pattern where the mantle is poorly developed or absent.

The contrasting relationship of the leucosomes with the S_2 fabric supports at least two discrete melting events, with biotite melting after the S_2-forming deformational event, either during M_{2b} or during the later decompression event (M_3). The thin cordierite-bearing veins resulted from the reaction

$$\text{biotite} + \text{aluminosilicate} + \text{quartz} = \text{cordierite} + (\text{K-feldspar}) + \text{L}_3 \quad (3)$$

probably during the M_3 decompression. Textural evidence for this reaction consists of ragged biotite inclusions within cordierite grains. Experimental studies show that the biotite dehydration-melting is expected to occur at temperatures >800°C and at pressures >7–8 kbar (Clemens & Vielzeuf, 1987; Le Breton & Thompson, 1988; Vielzeuf & Holloway, 1988; Carrington & Harley, 1995). We will demonstrate below that the *P–T* conditions of metamorphism in the studied area were conducive for dehydration-melting of biotite-bearing protoliths.

The amount of melt produced by dehydration-melting of biotite depends on (1) the amount of biotite in the protolith, (2) the temperature range over which melting occurs, (3) bulk rock X_{Mg}, (4) the solubility of water in the melt, which itself is a function of pressure, and (5) the diffusivity of Al (Clemens & Vielzeuf, 1987; Le Breton & Thompson, 1988; Vielzeuf & Holloway, 1988; Patino Douce & Johnston, 1991; Carrington & Harley, 1995). Therefore, melting of biotite-bearing protoliths is expected to occur over a range of temperature (Carrington & Harley, 1995). Under favourable conditions, biotite melting can produce up to 45% of melt at 850–860°C (references as above). We, therefore, argue that a substantial amount of melt was probably produced through biotite melting during the M_2 phase or during M_3 decompression at a nearly constant temperature. Because the thermal stability of biotite is expanded as a result of incorporation of Ti and F (Vielzeuf & Holloway, 1988), biotite was not completely consumed in the studied rocks. Melt fractions, exceeding the theoretical critical melt fraction (Arzi, 1978; Van der Molen & Patterson, 1979; Wickham, 1987), migrated from the site of melting to produce the discordant granitic leucosomes, veins and patches. It is likely that the melts formed during M_2 and M_3 may have accumulated in sufficient volumes at deeper levels to form pools, and were later emplaced as bodies of leucogranites. Leucogranite formation through vapour-absent melting of kyanite-grade metasedimentary protoliths at the base of the HHC have been suggested earlier

by some workers (e.g. Harris & Massey, 1994). Inger & Harris (1993), on the basis of geochemical constraints, considered the tourmaline leucogranites to represent low fraction (~12%) minimum melts generated through fluid-absent melting of micas, effectively removed from their source regions through deformation-enhanced processes. Scaillet *et al.* (1990) have experimentally shown that crystallization of tourmaline is favoured by low initial X_{H_2O} (<0·7), whereas at higher X_{H_2O}, biotite is the liquidus phase and tourmaline dissolves incongruently. Convective homogenization of higher melt fractions (>40%), with variable water activities, could produce the biotite leucogranites.

In the upper part of the HHC sequence, spinel + quartz appears in assemblages in localized patches during the M_3 phase. Textural features such as spinel–quartz intergrowths that rim sillimanite and garnet suggest the reaction

$$\text{garnet} + \text{sillimanite} = \text{spinel} + \text{quartz}. \quad (4)$$

Locally, these spinel–quartz symplectites are overgrown by plagioclase. Both this texture and lobate contacts between hercynite and quartz suggest later retrograde reactions (see Waters, 1991). Another expression of decompression in the pelitic rocks during M_3 is the formation of cordierite rims on garnet by the reaction

$$\text{garnet} + \text{sillimanite} + \text{quartz} = \text{cordierite}. \quad (5)$$

Evidence for the late stage (M_4) resorption of garnet through textural features such as embayed garnet margins against biotite and sillimanite is probably related to the net-transfer reaction

$$\text{garnet} + \text{K-feldspar} + H_2O = \text{biotite} + \text{sillimanite} + \text{quartz}. \quad (6)$$

The presence of intergrowths of biotite–quartz and biotite–sillimanite against garnet suggests the melt–solid interaction

$$\text{garnet} + (\text{K-feldspar}) + \text{melt} = \text{biotite} + \text{sillimanite} + \text{quartz}. \quad (7)$$

Calc-silicate rocks

There are no textural clues to the formation of clinopyroxene, but its appearance may be linked with the elimination of tremolite from the assemblages at an early stage of M_{2a} through the dehydration–decarbonation reaction

$$\text{calcite} + \text{tremolite} + \text{quartz} = \text{clinopyroxene} + H_2O + CO_2. \quad (8)$$

Textural features suggest the formation of scapolite through the M_{2a} prograde reaction

$$\text{calcite} + \text{plagioclase} = \text{scapolite}. \quad (9)$$

Development of porphyroblastic garnet also took place in the prograde path at the expense of calcite, anorthite (in plagioclase) and quartz via the model reaction

$$\text{anorthite} + \text{calcite} + \text{quartz} = \text{garnet} + CO_2. \quad (10)$$

This is supported by the presence of plagioclase, calcite and quartz inclusions in garnet. Breakdown of porphyroblastic garnet in the calc-silicate rocks is associated with M_3 decompression through the reaction

$$\text{garnet} + \text{calcite} + \text{quartz} = \text{clinopyroxene} + \text{plagioclase} + CO_2 \quad (11)$$

which is inferred from clinopyroxene$_2$–plagioclase$_2$ symplectites around garnet grains. The significant increase in CaTs and FeTs components in clinopyroxene$_2$ compared with matrix grains, and the depletion of andradite component in rims of porphyroblastic garnet grains suggest involvement of grossular and andradite components in reaction (11).

These rocks also show evidence of M_4-stage hydration, which led to the formation of phlogopite grains and amphibole rims on clinopyroxene.

Metabasites

The metabasic rocks rarely preserve evidence of their prograde history. Their textural and compositional characteristics suggest that the peak metamorphic assemblage consisted of hornblende + plagioclase + clinopyroxene ± garnet. The presence of garnet was apparently controlled by lower X_{Mg} in the bulk composition.

The M_3 decompression history of these rocks can be deciphered from reaction textures and mineral composition. Garnet broke down to orthopyroxene–plagioclase intergrowths through the reaction

$$\text{garnet} + \text{quartz} = \text{orthopyroxene} + \text{plagioclase}. \quad (12)$$

The progress of this reaction should deplete X_{Al} in orthopyroxene, X_{Gr} in garnet rims, features that are observed in the metabasites. Another retrogression feature is the partial conversion of orthopyroxene to anthophyllite.

GEOTHERMOBAROMETRY

Temperature was estimated using Fe–Mg partitioning between coexisting garnet and biotite in pelitic rocks. Several models for this thermometer are available

(Thompson, 1976; Goldman & Albee, 1977; Ferry & Spear, 1978; Hodges & Spear, 1982; Perchuk & Lavrenteva, 1983; Ganguly & Saxena, 1984; Indares & Martignole, 1985; Dasgupta *et al.*, 1991). Like all other Fe–Mg exchange thermometers, the garnet–biotite thermometer is likely to be reset during cooling (see Spear, 1991, 1992), and, therefore, may give temperatures lower than the peak values. The experimentally calibrated model of Ferry & Spear (1978) does not take into consideration the presence of Al^{VI} and Ti in natural biotite. The formulation of Dasgupta *et al.* (1991) takes into account the non-ideality in quaternary Fe–Mg–Mn–Ca garnet solid solution associated with mixing of Al and Ti in octahedral sites in biotite and was found to give consistent results for both amphibolite and granulite facies rocks. Considering that Al^{VI} and Ti are present in HHC biotites (Table 1), we have used this model to compute temperature. For comparison, we have also used the model of Ferry & Spear (1978). Applegate & Hodges (1994) showed that the most consistent temperatures are obtained when a combination of the quaternary garnet solid solution model of Berman (1990) and the biotite mixing parameters of Patino Douce *et al.* (1993) are used. Ganguly *et al.* (1996) have recently determined the activity–composition relationships in quaternary garnet solid solutions based on well-reversed experiments. We have, additionally, computed temperatures with a version of garnet–biotite thermometer (J. Ganguly, personal communication, 1997) that uses the experimentally derived garnet solution model of Ganguly *et al.* (1996) and the biotite solution model of Patino Douce *et al.* (1993). The results of the calculation are given in Table 4. We have arranged the samples according to their increasing distance from the MCT, and hence from the lowest to the highest structural levels.

Maximum temperatures were obtained using garnet core and matrix biotite compositions in all the models. However, the absolute values varied in the range 727–945°C (Ferry & Spear, 1978), 697–820°C (Dasgupta *et al.*, 1991) and 720–970°C (J. Ganguly, personal communication, 1997) from the lowest to the highest structural levels. Although it is not clear with which biotite composition garnet cores equilibrated, it is believed that a garnet core–matrix biotite combination is most likely to preserve temperatures close to the metamorphic peak (see Indares & Martignole, 1985). The Dasgupta *et al.* (1991) model consistently gave lower values than the other two. Both the Dasgupta *et al.* (1991) and J. Ganguly (personal communication, 1997) models gave results showing minimum scatter (± 25°C for closely associated samples at a particular structural level). However, the maximum temperature estimated by the Dasgupta *et al.* model (~820°C) from samples at the highest structural level is more consistent with the phase assemblages in metapelites (biotite–spinel–quartz–cordierite) and calc-silicate rocks (scapolite–calcite–plagioclase) at this level. We have, therefore, adopted the temperature estimates from the Dasgupta *et al.* (1991) model in this work.

Temperatures calculated for garnet rims against biotite are generally ~100°C lower than the garnet core–matrix biotite temperatures. The former represents cooling of the rocks. Using the experimental calibration of the equilibrium hercynite + quartz = garnet + sillimanite of Bohlen *et al.* (1986), with the activity models of Berman (1990) and Ganguly *et al.* (1996) for garnet, and that of Waters (1991) for hercynite, and assuming pressures of 5–6 kbar, we estimate temperatures around 820–850°C from the rim composition of garnet for the decompressive event.

Thermometers based on Fe–Mg partitioning between garnet–hornblende (Graham & Powell, 1984) and garnet–orthopyroxene (Harley, 1984; Lee & Ganguly, 1988; Bhattacharya *et al.*, 1991) were applied to the associated metabasic rocks. Temperatures calculated from the metabasic rocks (Table 5) show a fair agreement with those from the pelitic rocks at corresponding structural levels. Temperatures from garnet (core) and hornblende pairs range from 607 to 738°C. As orthopyroxene occurs as a late breakdown product of garnet, we used garnet rim compositions with orthopyroxene. However, we obtained higher temperatures, varying between 698 and 780°C (Harley, 1984), 865 and 926°C (Lee & Ganguly, 1988), and 735 and 787°C (Bhattacharya *et al.*, 1991). Temperatures given by the Harley (1984) model closely correspond to those obtained from metapelites at the same structural level.

A further temperature estimate can be obtained from the calc-silicate rocks utilizing the vapour-absent reaction anorthite + calcite = meionite, which is nearly independent of pressure. Using the formulation of Baker & Newton (1995) and the compositional characteristics of scapolite and plagioclase in the calc-silicate rocks, we obtain temperatures varying from 820 to 870°C. This estimate is consistent with those obtained from garnet core–matrix biotite temperatures in the pelitic rocks (Table 4).

Determination of pressure estimates for the pelitic rocks is complicated by the lack of pressure-sensitive assemblages in the Higher Himalayan Zone and is based mainly on the GASP barometer, which has been refined by Koziol & Newton (1988). In our calculations, we have used the Berman (1990) activity model for, garnet, and the Elkins & Grove (1990) model for plagioclase, as a combination of these two models has been shown to yield pressure estimates consistent with the stabilities of the Al_2SiO_5 polymorphs (see Applegate & Hodges, 1994). Using the Ganguly *et al.* (1996) model for garnet, we obtained nearly identical results. The calculated pressures are given in Table 4. Some degree of uncertainty in

Table 4: Result of geothermobarometry in metapelites

Sample	Structural	Cores						Rims					
	distance from	*T* (°C)			*P* (kbar)			*T* (°C)				*P* (kbar)	
	MCT (km)	GARB			GASP		GRAIL	GARB			GC	GASP	G
		FS	D	G	KN	G	GS	FS	D	G	B	KN	G
9/89	9·6	727	697	720	7·4	8·1	—	609	632	610	—	4·3	4·5
9/89	9·6	812	697	740	6·0	8·0	—	672	577	600	—	4·1	4·2
9/89	9·6	843	702	728	—	—	—	—	—	—	—	—	—
699/87	12·8	*	*	*	7·7	8·2	—	677	630	645	—	6·6	6·8
699/87	12·8	*	*	*	8·0	8·5	—	*	*	*	—	5·7	5·4
108/88	12·8	912	743	820	8·4	7·5	—	580	551	573	—	5·8	6·2
2/89	14·7	838	701	856	9·9	8·9	—	602	580	625	—	—	—
2/89	14·7	854	740	860	9·7	9·1	—	—	588	646	—	3·8	4·2
2/89	14·7	860	743	830	—	—	—	626	561	624	—	4·6	5·0
2/89	14·7	860	744	830	10·2	10·4	—	814	679	740	—	6·1	5·8
113/88	14·7	*	784	815	9·7	10·0	—	811	690	705	690	5·9	6·1
726/87	16	868	726s	910	7·5	7·2	6·4	806	687	790	—	6·8	6·1
726/87	16	—	—	—	8·8	8·9	—	709	607	653	—	3·8	4·2
726/87	16	—	—	—	11·0	11·6	—	—	—	—	—	4·06	3·9
115/88	16	945	757	880	9·3	8·7	—	802	634	765	—	4·2	5·1
115/88	16	*	794	*	—	—	—	—	—	—	—	—	—
115/88	16	925	712	890	9·0	9·8	—	674	521	647	—	3·0	*
20/89B	27·6	816	768	822	11·8	10·1	—	810	717	705	—	4·7	4·5
20/89A	27·6	836	793	834	12·1	11·3	—	781	697	685	—	—	—
20/89A	27·6	889	770	844	—	—	—	798	695	700	—	5·8	6·3
20/89A	27·6	920	814	870	10·05	11·1	—	—	—	—	—	5·5	5·9
64/86	32	901	806	970	10·8	11·8	—	—	—	—	—	4·4	5·8
64/86	32	—	—	—	14·3	13·6	—	854	737	907	—	8·2	7·6
64/86	32	913	820	933	11·7	12·1	—	855	747	862	—	7·1	8·4

*Abnormal temperature estimate (see text).
—, not calculated. FS, Ferry & Spear (1978); D, Dasgupta *et al.* (1991); B, Bhattacharya *et al.* (1988); KN, Koziol & Newton (1988); G, after Ganguly *et al.* (1996), Elkins & Grove (1990) and Patino Douce *et al.* (1993), see text for discussion. GS, Ganguly & Saxena (1984). s, small grain; GARB, garnet–biotite; GC, garnet–cordierite; GASP, garnet–aluminosilicate–plagioclase–quartz; GRAIL, garnet–rutile–aluminosilicate–ilmenite–quartz.

pressure determination arises from difficulties in retrieving mineral compositions that represent the metamorphic peak. Pressures obtained using garnet cores and matrix plagioclase range from 8·8 to 11·8 kbar. Garnet rim compositions and adjacent plagioclase grains yield a drop in pressure of about 4–6 kbar, indicating decompression during retrograde metamorphism.

The garnet–hornblende–plagioclase–quartz (Kohn & Spear, 1990), garnet–rutile–ilmenite–plagioclase–quartz (GRIPS, Bohlen & Liotta, 1986) and garnet–orthopyroxene–plagioclase–quartz (Perkins & Chipera, 1985; Bhattacharya *et al.*, 1991) barometers were applied to the metabasites. The results are given in Table 5. We derive pressures varying from 5·6 to 8·5 kbar in the different formulations.

CONDITIONS OF METAMORPHISM

Spear (1991, 1992) and Spear & Florence (1992) highlighted the problems of interpreting metamorphic temperatures related to mineral reaction history, garnet grain size, modal proportions and cooling rates on the deduced *P*–*T* values. The Higher Himalayan garnets show textures

Table 5: Result of geothermobarometry in metabasites

Sample	Structural distance from MCT (km)	Cores			Rims		
		T (°C)		*P* (kbar)	*T* (°C)		*P* (kbar)
		GARH	GHSP	GRIPS	GARH	GO	GOPS
642/87	8·3	577	5·6	—	625		—
642/87	8·3	—	6·1	—	—	—	
665/87	9·6	600	6·6	7·7		—	—
690/87	11·6	737	7·0	—	650	735(B)	6·4(P)
690/87	11·6	—	—	—	—	865(L)	7·6(B)
690/87	11·6	—	—	—	—	701(H)	—
97/88	12·2	690	7·0	—	—	—	—
97/88	12·2	—	7·5	—	—	—	—
88/88	23	623	7·0	8·5	622	—	—

—, not determined. GARH, garnet–hornblende thermometer of Graham & Powell (1984); GO, garnet–orthopyroxene thermometer; H, Harley (1984); L, Lee & Ganguly (1988); B, Bhattacharya *et al.* (1991); GRIPS, garnet–rutile–ilmenite–plagioclase–quartz barometer of Bohlen & Liotta (1986); GHSP, garnet–plagioclase–quartz–hornblende geobarometer of Kohn & Spear (1990); GOPS, garnet–plagioclase–orthopyroxene–quartz geobarometer; P, Perkins & Chipera (1985); B, Bhattacharya *et al.* (1991).

and zoning patterns which suggest retrograde exchange and net transfer reactions. Thus, results of thermobarometry should show departure from peak values. Temperatures obtained from garnet–biotite thermometry (Ferry & Spear, 1978) are scattered and some samples yield unrealistically high values. This is attributed to non-ideal mixing in garnet and the presence of appreciable Ti and Al^{VI} in biotite. These higher T values have been omitted and the corresponding values for the Dasgupta *et al.* (1991) formulation are used instead. Higher temperatures were obtained for some samples by all the models, using garnet core and matrix biotite compositions (e.g. Sample 699/87, Table 4). The volumetric ratio of garnet to biotite is very low in these samples. Post-peak modification of biotite composition to higher Fe/Mg ratios, possibly because of the operation of retrogressive net-transfer reactions, may account for higher estimated temperatures (see Spear & Florence, 1992). None the less, we have obtained some of the highest P–T estimates from the Higher Himalayan domain based on both thermobarometry and mineral assemblages. Peak M_2 P–T conditions were probably 10–12 kbar and 800–850°C.

A hercynite–quartz zone is present in the uppermost part of the Central Crystalline sequence in Sikkim. Swapp & Hollister (1991) have described earlier a hercynite–quartz–sillimanite-bearing metapelite from adjoining Bhutan Himalayas. The occurrence of Fe–Mg spinel and quartz in pelitic rocks implies very high temperatures and an elevated thermal gradient at mid- to lower-crustal levels, as reported from a number of granulite terrains (Waters, 1991). We assign the breakdown of porphyroblastic garnet to spinel and quartz in the pelites to the M_3 decompressive event. Bohlen *et al.* (1986) experimentally calibrated the stability field of the assemblage hercynite–quartz, which is extended to lower temperatures by gahnite and magnetite, and showed a positive dP/dT, centred around 880 and 1020°C at 5·2–5·4 and 8·6–8·8 kbar, respectively. High $f(O_2)$ also has the effect of increasing the stability field of hercynite + quartz. In our samples X_{Mg} in spinel is slightly less than that in garnet (Table 1). Sengupta *et al.* (1991) argued that high Fe/Mg ratios in the bulk composition and large amounts of Zn in spinel can override the effect of $f(O_2)$. At high T and low P, X_{Mg} in spinel could be less than that for garnet. The spinel–quartz-bearing assemblage in the HHC is, therefore, indicative of high-T decompression.

For comparison with other studies in adjoining areas (Hubbard, 1989; Swapp & Hollister, 1991; Inger & Harris, 1992) we have arranged the samples according to their distance from the MCT, notwithstanding the diversity of opinions regarding the exact location of the MCT in Sikkim (Lal *et al.*, 1981; SinhaRoy, 1982). We find an excellent correlation between increasing temperature and pressure and higher structural levels (Fig. 18a and b). A difference of ~125°C is seen over a structural distance of 22·5 km, corresponding to an anomalously low thermal gradient of 5·5°C/km. We expect the temperatures to have been buffered to a large extent by melting in the HHC pile (see Hodges *et al.*, 1988). In spite of greater uncertainties in pressure determination, a gradient of 0·25 kbar/km is inferred, resembling a normal lithostatic gradient of ~0·28 kbar/km.

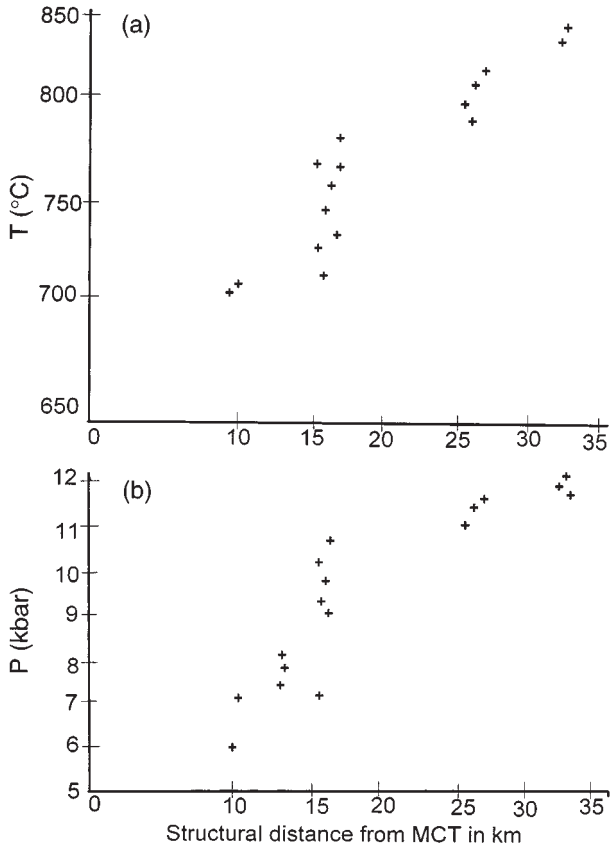

Fig. 18. Plot showing the variation of temperature (a) and pressure (b) with structural distance from the MCT.

Comparison of our available P–T estimates and profiles of the upper HHC with those from the MCT zone and sillimanite isograd in Sikkim, as well as from adjoining areas in Nepal and Bhutan, reveals significant differences. The thermobarometric data of Mohan *et al.* (1989) from Sikkim also show increasing pressure and temperature from the staurolite to the sillimanite zone, with the exception of garnet zone samples which record higher pressure. Because our study began from the sillimanite zone of Mohan *et al.* (1989) and ranged to higher structural levels, the maximum temperatures recorded in this study exceed those reported by them, as well as those from Bhutan by Swapp & Hollister (1991), by as much as 100°C. Hubbard (1989) reported an increase in temperature towards higher structural levels through the MCT zone in Nepal, and then a decrease at middle levels. Her pressure estimates resemble a normal lithostatic gradient. Major variations are seen in P–T profiles reported by different workers even within a single area. In the Langtang Valley of Nepal, Macfarlane (1995) demonstrated a decrease in pressures towards upper structural levels but did not detect any variation in temperature. In the same area, Inger & Harris (1992) noted a clustering of high-T estimates towards the top of the section and a drop in pressure, confirming the continuation of the inverted metamorphic zonation into the HHC. We could cite a number of reasons for the variations, without discounting the possibility that some of these differences could be real and not just artefacts of calculation procedures. Prima facie, the major reason appears to be the different solution models and calibrations used in the various studies. We suggest that relative P–T values obtained from a particular method are readily compared and, therefore, the P–T gradients we have obtained are probably robust. It can be readily seen from Tables 4 and 5 and Fig. 18a and b that both P and T increase progressively towards the upper structural levels from the MCT zone. The mineral assemblages and other field observations support the recorded P–T gradient in the HHC pile. The temperature gradient is corroborated by elimination of muscovite at the lower HHC, the progressive increase in melt fractions towards higher structural levels, and the appearance of assemblages with spinel and quartz (indicative of high-temperature decompression) only at the highest structural levels. Rather than a true reverse metamorphic zoning where high-T rocks are exposed at higher structural levels, our P–T profile for the HHC in Sikkim shows an increase in both pressure and temperatures towards shallower structural levels, which indicates an inverted Barrovian sequence.

DISCUSSION

The prolonged metamorphic history for the HHC we have inferred from textural and compositional zoning characteristics is divided into distinct segments representing the tectonothermal evolution of the region. Our P–T path for the HHC, constrained by mineral reaction history and thermobarometric estimates for the different episodes of mineral growth, is shown in a P–T grid (Fig. 19), which also depicts the experimentally determined reaction equilibria relevant to the present study.

Recent studies in the Himalayas have emphasized a polymetamorphic history of the Lesser and Higher Himalayan rocks (Brunel & Kienast, 1986; Hodges & Silverberg, 1988; Hodges *et al.*, 1988; Pecher, 1989; Staubli, 1989; Swapp & Hollister, 1991; Inger & Harris, 1992; Macfarlane, 1995). Complex textural and mineral zoning features have been described from northwest Pakistan (Treloar *et al.*, 1989), Kistwar in northwestern India (Staubli, 1989) and Bhutan (Swapp & Hollister, 1991). Our study has yielded fairly conclusive evidence for multi-episodic growth of different porphyroblastic phases. Two episodes of prograde metamorphism, M_1 and M_2, have been suggested by many workers in their respective areas (e.g. Brunel & Kienast, 1986; Swapp &

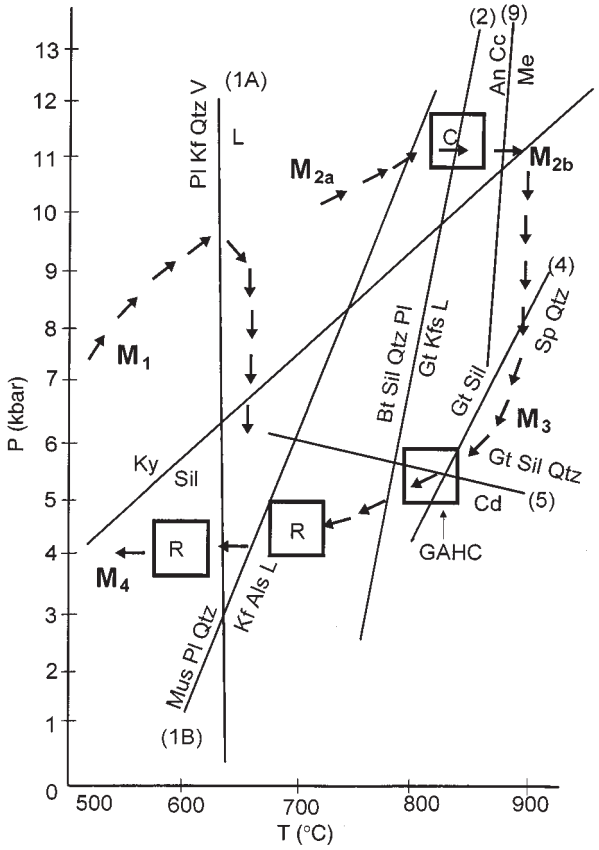

Fig. 19. Pressure–temperature evolutionary path for rocks in the upper part of the HHC. M_1, M_2, M_3 and M_4 are the phases of metamorphism as discussed in the text. Boxes indicate geothermobarometric estimates (garnet–biotite thermometer and GASP barometer) from different samples in the HHC using core (C) and rim (R) compositions. Boxes also indicate the uncertainties in the estimates. The box GAHQ is calculated after Bohlen *et al.* (1986). Reaction (1A) is from Vielzeuf & Holloway (1988), reactions (1B) and (2) are from Le Breton & Thompson (1988) and reaction (5) is from Thompson (1976), adjusted for natural composition. Reaction (9) has been computed from Baker & Newton (1995).

Hollister, 1991; Hodges *et al.*, 1994), although they differ as to their timing, mechanism and relation to deformational episodes. For Sikkim, we infer a period of heating and decompression for the M_1 event (Fig. 19), based on zoning patterns of the inner parts of composite garnets which show rimward increase in X_{Py} and X_{Sp} and depletion of X_{Gr} with calcic plagioclase mantles. There is, however, no way of determining quantitative P–T estimates of the peak M_1 conditions. This is due to the difficulty of identifying M_1 equilibrium assemblages owing to overprinting by the later, dominant M_2 event. Temperatures may have reached those of partial melting because of the relict leucocratic layers that define rootless, early F_2 fold hinges. The timing of the M_1 metamorphic event is uncertain, reflecting a lack of reliable geochronological constraints on the age of the main marker fabric (S_2). Although a Precambrian or Palaeozoic age has been suggested from several areas (Chamberlain *et al.*, 1989; Pognante & Lombardo, 1989; Metcalfe, 1993; Oliver *et al.*, 1995), most of the data appear to converge towards an early Tertiary age (e.g. Inger & Harris, 1992, 34 Ma; Hodges *et al.*, 1994, 25 Ma; Hodges *et al.*, 1996, early Oligocene; Brunel & Kienast, 1986; Hodges & Silverberg, 1988; Hodges *et al.*, 1988; Pecher, 1989).

The results of thermobarometry and the inferred P–T evolution of the HHC suggest that the Indian plate rocks may have undergone renewed burial during the initial stages of collision, leading to the syn-collisional prograde metamorphic event M_2 (Fig. 19). We relate the syntectonic M_{2a} stage with muscovite dehydration melting primarily on two considerations: (1) the small volumes of melts produced by muscovite melting would probably be unable to migrate from their site of generation, and (2) the leucosomes are conformable to the S_2 fabric and preserve only the post-D_2 deformation (such as layer parallel stretching). The subsequent stage, M_{2b}, shows a trend towards higher T as the rocks recrystallized under static conditions, resulting in dehydration melting of biotite, close to T_{Max}. A relatively flat (low dP/dT) gradient has been inferred for this segment based on Ca zoning in the post-tectonic rims of composite garnets. It is unlikely that such flat Ca patterns are due to relaxation zoning, because patterns for Mg and Fe are more or less preserved. Well-constrained isotopic age data indicate an age between 20 and 22 Ma for the M_2 event (Hubbard & Harrison, 1989; Pecher, 1989; Parrish *et al.*, 1992; Macfarlane, 1993, 1995; Harris & Massey, 1994; Hodges *et al.*, 1994).

The M_3 event represents the post-peak exhumation history of the HHC. It is recorded by the ubiquitous breakdown of porphyroblastic garnet in all the lithologies. Garnet reacted to form cordierite and spinel–quartz intergrowths in the pelitic rocks, orthopyroxene–plagioclase symplectites in the metabasites, and clinopyroxene–plagioclase in the calc-silicates. Such reactions (with the exception of that forming spinel + quartz) are observed in all the structural levels of the HHC. This episode, characterized by near-isothermal decompression, occurred in response to rapid uplift and erosion. Exhumation may have been synchronous with movement on the South Tibetan Detachment System, bracketed between 17 and 20 Ma in Nepal (Copeland & Harrison, 1987; Parrish *et al.*, 1992; Macfarlane, 1993) and between 13 and 16 Ma in Tibet (Hodges *et al.*, 1994). The late-stage retrogressive event (M_4) reflects the final cooling and hydration of the rocks under low-grade conditions, which resulted in extensive breakdown of the prograde phases and overprinting by retrogressive assemblages.

The inferred clockwise P–T path of the post-M_1 segment of the HHC (Fig. 19) resembles the type modelled

by England & Thompson (1984) for crustal thickening by overthrusting. The M_2 event would, then, pertain to the heating following thickening as a result of the thermal relaxation towards a steady-state geotherm, and may have been followed by a gap of a few million years between the thickening and beginning of exhumation, represented by the interkinematic M_{2b} event. It remains to be seen whether the reported high temperatures can be obtained through crustal thickening alone. Simple one-dimensional modelling by Harris & Massey (1994) does not favour attainment of such high temperatures solely through thermal relaxation. Thermal relaxation models also fail to account for the continuous inverted metamorphic zonation from the MCT zone to the upper parts of the HHC. We also rule out selective heating of the upper part of the HHC by heat focusing during M_2, as proposed by Inger & Harris (1992), on the grounds that M_2 was recorded at the base of the HHC in Sikkim and the deduced P–T profile is inconsistent with such a mechanism. Other possible sources of heat include shear heating along thrust faults (England & Molnar, 1993) and heat advection because of leucogranite intrusions into the HHC (e.g. Hollister *et al.*, 1995). The latter possibility is not directly applicable to the present area because we interpret the leucogranites to be the product of M_2 metamorphism. Although a number of shear zones have been mapped in Sikkim and it is likely that some amount of localized heating may have taken place in the vicinity of these zones, on a broader scale this model fails to account for the observed P–T gradients in the area. Swapp & Hollister (1991), from their study in the Bhutan Himalaya, developed a model of tectonic transport of heat from the lower crust into the middle crust because of melt-induced thrusting of high-grade migmatitic rocks onto lower-grade rocks. Interestingly, this model would predict higher metamorphic pressures at upper structural levels (fig. 6, Swapp & Hollister, 1991).

Intrinsically coupled with the problem of source of heat for the high-grade metamorphism in the Himalayas is the occurrence of inverted metamorphic zones. Inverted metamorphic sequences may or may not represent inverted crustal isotherms (e.g. Jamieson *et al.*, 1996). In the former case, it is implicit that the pattern of metamorphic isograds exposed at the surface records the distribution of crustal isotherms at the time of metamorphism. Models falling in this category include (1) the 'hot-iron model' (Le Fort, 1975, 1981), and (2) dissipative heating along thrusts (Graham & England, 1976; Barton & England, 1979; England & Molnar, 1993). If the observed metamorphic zonation is a result of thrusting of a hot deeper crustal slab over the cooler Lesser Himalayan rocks (Le Fort, 1975), it would be difficult to explain how the hanging wall slab could show increasing pressure and temperature towards shallower levels. Furthermore, the observed metamorphic zonation is not consistent with dissipative heating along thrusts. Several other models have been proposed which consider that the inverted zones do not represent inverted isotherms. These include (1) post-metamorphic imbricate thrusting of a normally metamorphosed pile in a manner that stacks progressively higher-grade rocks on top of lower-grade ones (Treloar *et al.*, 1989), (2) tectonic inversion by folding (Searle *et al.*, 1988; Searle & Rex, 1989), (3) tectonic juxtaposition of higher- and lower-grade rocks during or soon after metamorphism (Swapp & Hollister, 1991); (4) syn-metamorphic ductile shearing (Jain & Manickavasagam, 1993; Grujik *et al.*, 1996; Jamieson *et al.*, 1996; Davidson *et al.*, 1997), and (5) tectonic inversion of isograds by displacement along shear zones (Brunel & Kienast, 1986; Reddy *et al.*, 1993). The models (1), (2), (3) and (4) would predict progressive increase in both pressure and temperature towards higher structural levels, as recorded in this work. At the present level of observation in the Sikkim Himalayas it is not possible to select one of the above models as the cause of inversion of the studied metamorphic sequence.

ACKNOWLEDGEMENTS

The present work forms a part of the doctoral work of S. N. We thank Himadri Banerjee and Pulak Sengupta for many valuable suggestions. S. D. acknowledges some very useful discussions with Sumit Chakraborty. Professor J. Ganguly kindly provided a version of his unpublished garnet–biotite thermometer. We are grateful to Dr K. V. Hodges, Dr L. S. Hollister and Dr R. J. Tracy for their very constructive and helpful suggestions on an earlier version of the paper. We thank Dr S. Sorensen for giving helpful suggestions and for her thorough editorial work, which improved the presentation of the paper. S. N. and S. D. are thankful to their wives, Rupa and Keya, respectively, for graciously and uncomplainingly accepting the long absence of their husbands during the field-work in Sikkim. S. N. thanks the Director General, Geological Survey of India, for permission to carry out the work. S. D. was a grateful recipient of a Research Fellowship from the Alexander von Humboldt Foundation, when the last version of the paper was prepared.

REFERENCES

Applegate, J. D. R. & Hodges, K. V., (1994). Empirical evaluation of solution models for pelitic minerals and their application to thermobarometry. *Contributions to Mineralogy and Petrology* **117,** 56–65.

Arzi, A. A., (1978). Critical phenomena in the rheology of partially melted rocks. *Tectonophysics* **44,** 173–184.

Baker, J. & Newton, R. C., (1995). Experimentally determined activity–composition relations for Ca-rich scapolite in the system $CaAl_2Si_2O_8$–$NaAlSi_3O_8$–$CaCO_3$ at 7 kbar. *American Mineralogist* **80,** 744–751.

Banerjee, H., Dasgupta, S., Bhattacharya, P. K. & Sarkar, S. C., (1983). Evolution of the Lesser Himalayan metapelites of the Sikkim–Darjeeling region, India, and some related problems. *Neues Jahrbuch fur Mineralogie* **142,** 199–222.

Barnicoat, A. C. & Treloar, P. J., (1989). Himalayan metamorphism—an introduction. *Journal of Metamorphic Geology* **7,** 3–8.

Barton, C. M. & England, P. C., (1979). Shear heating at the Olympos (Greece) thrust and the deformation properties of carbonates at geological strain rates. *Geological Society of America Bulletin* **90,** 483–492.

Berman, R. G., (1990). Mixing properties of Ca–Mg–Fe–Mn garnets. *American Mineralogist* **75,** 328–344.

Bhattacharya, A., Mazumdar, A. C. & Sen, S. K., (1988). Fe–Mg mixing in cordierite: constraints from natural data and implications for garnet–cordierite geothermometry in granulites. *American Mineralogist* **73,** 338–344.

Bhattacharya, A., Krishnakumar, K. K., Raith, M. & Sen, S. K., (1991). An improved set of *a–x* parameters for Fe–Mg–Ca garnets and refinements of the orthopyroxene–garnet thermometer and the orthopyroxene–garnet–plagioclase–quartz barometer. *Journal of Petrology* **32,** 629–656.

Bohlen, S. R. & Liotta, J. J., (1986). A barometer for garnet amphibolites and garnet granulites. *Journal of Petrology* **27,** 1025–1034.

Bohlen, S. R., Dollase, W. A. & Wall, V. J., (1986). Calibration and application of spinel equilibria in the system $FeO–Al_2O_3–SiO_2$. *Journal of Petrology* **27,** 1143–1156.

Brunel, M., (1986). Ductile thrusting in the Himalayas: shear sense criteria and stretching lineations. *Tectonics* **5,** 247–265.

Brunel, M. & Kienast, J. R., (1986). Etude petrostructurale des chevauchements ductile himalayens sur la transversale de L'Everest–Makalu (Nepal oriental). *Canadian Journal of Earth Sciences* **23,** 1117–1137.

Burchfiel, B. C., Zhiliang, C., Hodges, K. V., Yuping, L., Royden, L. H., Changrong, D. & Jiene, X., (1992). The South Tibetan Detachment system, Himalayan orogen: extension contemporaneous with and parallel to shortening in a collisional mountain belt. *Geological Society of America Special Paper* **269,** 41 pp.

Carrington, D. & Harley, S. L., (1995). Partial melting and phase relations in high grade metapelites: an experimental grid in the KFMASH system. *Contributions to Mineralogy and Petrology* **120,** 270–291.

Chamberlain, C. P., Zeitler, P. K. & Jan, M. Q., (1989). The dynamics of the suture between Kohistan island arc and the Indian plate in the Himalaya of Pakistan. *Journal of Metamorphic Geology* **7,** 135–149.

Clemens, J. D. & Vielzeuf, D., (1987). Constraints on melting and melt production in the crust. *Earth and Planetary Science Letters* **86,** 287–306.

Copeland, P. & Harrison, T. M., (1987). Constraints on the age of normal faulting, north face of Mt. Everest: implications for Oligocene–Miocene uplift. *EOS Transactions, American Geophysical Union* **68,** 1444.

Davidson, C., Grujik, D., Hollister, L. S. & Schmid, S. M., (1997). Metamorphic reactions related to decompression and synkinematic intrusion of leucogranite, High Himalayan Crystallines, Bhutan. *Journal of Metamorphic Geology* **15,** 593–612.

Elkins, L. T. & Grove, T. L., (1990). Ternary feldspar experiments and thermodynamic models. *American Mineralogist* **75,** 544–559.

England, P. C. & Molnar, P., (1993). The interpretation of inverted metamorphic isograds using simple physical calculations. *Tectonics* **12**(1), 145–157.

England, P. C. & Thompson, A. B., (1984). Pressure–temperature–time paths of regional metamorphism. I. Heat transfer during the evolution of regions of thickened continental crust. *Journal of Petrology* **25,** 894–928.

Ferry, J. M. & Spear, F. S., (1978). Experimental calibration of the partitioning of Fe and Mg between biotite and garnet. *Contributions to Mineralogy and Petrology* **66,** 113–117.

Ganguly, J. & Saxena, S. K., (1984). Mixing properties of aluminosilicate garnets: constraints from natural and experimental data and applications to geothermobarometry. *American Mineralogist* **69,** 88–97.

Ganguly, J., Cheng, W. & Tirone, M., (1996). Thermodynamics of aluminosilicate garnet solid solutions: new experimental data, an optimized model and thermometric applications. *Contributions to Mineralogy and Petrology* **126,** 137–151.

Gansser, A., (1964). *Geology of the Himalaya*. London: Interscience.

Gansser, A., (1983). Geology of the Bhutan Himalaya. *Denkschriften der Schweizerischen Naturforschenden Gesellschaft* **96,** 181 pp.

Goldman, D. S. & Albee, A. L., (1977). Correlation of Mg/Fe partitioning between garnet and biotite with $^{18}O/^{16}O$ partitioning between quartz and magnetite. *American Journal of Science* **277,** 750–767.

Graham, C. M. & England, P. C., (1976). Thermal regimes and regional metamorphism in the vicinity of overthrust faults: an example of shear heating and inverted metamorphic zonation from southern California. *Earth and Planetary Science Letters* **31,** 142–152.

Graham, C. M. & Powell, R., (1984). A garnet–hornblende geothermometer: calibration, testing and application to the Pelona schist, southern California. *Journal of Metamorphic Geology* **2,** 21–31.

Grujik, D., Casey, M., Davidson, C., Hollister, L. S., Kundig, R., Pavlis, T. & Schmid, S., (1996). Ductile extrusion of the Higher Himalayan Crystalline in Bhutan: evidence from quartz microfabrics. *Tectonophysics* **260,** 21–43.

Harley, S., (1984). An experimental study of partitioning of Fe and Mg between garnet and orthopyroxene. *Contributions to Mineralogy and Petrology* **86,** 359–373.

Harris, N. B. W. & Massey, J., (1994). Decompression and anatexis of Himalayan metapelites. *Tectonics* **13**(6), 1537–1546.

Harris, N. B. W., Inger, S. & Massey, J., (1993). The role of fluids in the formation of the High Himalayan leucogranites. In: Treloar, P. J. & Searle, M. P. (eds) *Himalayan Tectonics. Geological Society, London, Special Publication* **74,** 391–399.

Hodges, K. V. & Silverberg, D. S., (1988). Thermal evolution of the Greater Himalaya, Garhwal, India. *Tectonics* **7,** 583–600.

Hodges, K. V. & Spear, F. S., (1982). Geothermometry, geobarometry and the Al_2SiO_5 triple point at Mount Mousilake, New Hampshire. *American Mineralogist* **67,** 1118–1134.

Hodges, K. V., Hubbard, M. S. & Silverberg, D. S., (1988). Metamorphic constraints on the thermal evolution of the central Himalayan orogen. *Philosophical Transactions of the Royal Society of London, Series A* **326,** 257–280.

Hodges, K. V., Hames, W. E., Olszewiski, W. J., Burchfiel, B. C., Royden, L. H. & Chen, Z., (1994). Thermobarometric and $^{40}Ar/^{39}Ar$ geochronologic constraints on Eohimalayan metamorphism in the Dinggye area, southern Tibet. *Contributions to Mineralogy and Petrology* **117,** 151–163.

Hodges, K. V., Parrish, R. R. & Searle, M. P., (1996). Tectonic evolution of the Central Annapurna range, Nepalese Himalayas. *Tectonics* **15,** 1264–1291.

Hollister, L. S., Kundig, R., Schmid, S., Grujik, D., Pavlis, T. & Davidson, C., (1995). Tectonic transport of heat and melt within the High Himalayan Crystallines of Bhutan. In: Spencer, D. A., Burg, J. P. & Spencer-Cervato, C. (eds) *10th Himalaya Karakoram Tibet Workshop*. Zurich: Institut Technische Hochschule Universitat Zurich, **298,** 37–39.

Honegger, K., Dietrich, V., Frank, W., Gansser, A., Thoni, M. & Tromsdorff, V., (1982). Magmatism and metamorphism in the Ladakh Himalaya (the Indus–Tsangpo suture zone). *Earth and Planetary Science Letters* **60,** 253–292.

Hubbard, M. S., (1989). Thermobarometric constraints on the thermal history of the Main Central Thrust zone and Tibetan slab, Eastern Nepal Himalaya. *Journal of Metamorphic Geology* **7,** 19–30.

Hubbard, M. S. & Harrison, T. M., (1989). $^{40}Ar/^{39}Ar$ age constraints on deformation and metamorphism in the Main Central Thrust zone and Tibetan slab, eastern Nepal Himalaya. *Tectonics* **8,** 865–880.

Indares, A. & Martignole, J., (1985). Biotite–garnet geothermometry in granulite facies rocks: the influence of Ti and Al in biotite. *American Mineralogist* **70,** 271–278.

Inger, S. & Harris, N. B. W., (1992). Tectonothermal evolution of the higher Himalayan Crystalline sequence, Langtang valley, northern Nepal. *Journal of Metamorphic Geology* **10,** 439–452.

Inger, S. & Harris, N. B. W., (1993). Geochemical constraints on leucogranite magmatism in Langtang valley, Nepal Himalaya. *Journal of Petrology* **34,** 345–368.

Jain, A. K. & Manickavasagam, R. M., (1993). Inverted metamorphism in the intracontinental ductile shear zone during Himalayan collision tectonics. *Geology* **21,** 407–410.

Jamieson, R. A., Beaumont, C., Hamilton, J. & Fullsack, P., (1996). Tectonic assembly of inverted metamorphic sequences. *Geology* **24,** 839–842.

Kohn, M. J. & Spear, F. S., (1990). Two new geobarometers for garnet amphibolites with applications to southeastern Vermont. *American Mineralogist* **75,** 89–96.

Koziol, A. M. & Newton, R. C., (1988). Redetermination of the anorthite breakdown reaction and improvement of the plagioclase–garnet–Al_2SiO_5–quartz barometer. *American Mineralogist* **73,** 216–233.

Lal, R. K., Mukherjee, S. & Ackermand, D., (1981). Deformation and Barrovian metamorphism at Takdah, Darjeeling (Eastern Himalaya). In: Saklani, P. S. (ed.) *Metamorphic Tectonites of the Himalaya*. New Delhi: Today and Tomorrow Publishers, pp. 231–278.

Le Breton, N. & Thompson, A. B., (1988). Fluid-absent (dehydration) melting of biotites in metapelites in the early stages of crustal anatexis. *Contributions to Mineralogy and Petrology* **99,** 226–237.

Le Fort, P., (1975). Himalaya: the collided range. Present knowledge of the continental arc. *American Journal of Science* **275A,** 1–4.

Le Fort, P., (1981). Manaslu leucogranite: a collisional signature of the Himalaya, a model for its genesis and emplacement. *Journal of Geophysical Research* **86,** 10545–10568.

Lee, H. Y. & Ganguly, J., (1988). Equilibrium composition of coexisting garnet and orthopyroxene: experimental determinations in the system FeO–MgO–Al_2O_3–SiO_2 and applications. *Journal of Petrology* **29,** 93–113.

Lombardo, B., Pertusati, P. & Borghi, S., (1993). Geology and tectonomagmatic evolution of the eastern Himalaya along the Chomolungma–Makalu transect. In: Treloar, P. J. & Searle, M. P. (eds) *Himalayan Tectonics. Geological Society, London, Special Publication* **74,** 341–355.

Macfarlane, A. M., (1993). The chronology of tectonic events in the crystalline core of the Himalaya, Langtang National Park, Central Nepal. *Tectonics* **12,** 1004–1025.

Macfarlane, A. M., (1995). An evaluation of the inverted metamorphic gradient at Langtang National Park, Central Nepal Himalaya. *Journal of Metamorphic Geology* **13,** 595–612.

Metcalf, R. P., (1993). Pressure, temperature and time constraints on metamorphism across the Main Central Thrust zone and High Himalayan slab in the Garhwal Himalayas. In: Treloar, P. J. & Searle, M. P. (eds) *Himalayan Tectonics. Geological Society, London, Special Publication* **74,** 485–509.

Mohan, A., Windley, B. F. & Searle, M. P., (1989). Geothermobarometry and development of inverted metamorphism in the Darjeeling–Sikkim region of the eastern Himalaya. *Journal of Metamorphic Geology* **7,** 95–110.

Molnar, P., (1986). The geologic history and structure of the Himalaya. *American Scientist* **74,** 143–154.

Oldham, R. D., (1883). Notes on a traverse between Almora and Mussooree in October, (1882). *Geological Survey of India Reconnaissance* **16,** 162–164.

Oliver, G. J. H., Johnson, M. R. W. & Fallick, A. E., (1995). Age of metamorphism in Lesser Himalaya and Main Central Thrust zone, Garhwal, India: results of illite crystallinity, $^{40}Ar/^{39}Ar$ fusion and K–Ar studies. *Geological Magazine* **132,** 139–149.

Parrish, R. R. & Hodges, K. V., (1996). Isotopic constraints on the age and provenance of the Lesser and Greater Himalayan sequences, Nepalese Himalayas. *Geological Society of America Bulletin* **108,** 904–911.

Parrish, P. R., Hodges, K. V. & Macfarlane, A. M., (1992). A U–Pb geochronology of the igneous and metamorphic rocks near the Main Central Thrust in the Langtang area, Central Nepal Himalaya. *7th Annual Himalaya–Karakoram–Tibet Workshop*, Oxford, UK, April (1992).

Patiño Douce, A. E. & Johnston, A. D., (1991). Phase equilibria and melt productivity in the pelitic system: implications for the origin of peraluminous granitoids and aluminous granulites. *Contributions to Mineralogy and Petrology* **109,** 202–218.

Patiño Douce, A. E., Johnston, A. D. & Rice, J. M., (1993). Octahedral excess mixing properties in biotite: a working model with applications to geobarometry and geothermometry. *American Mineralogist* **78,** 113–131.

Patriat, P. & Achache, J., (1984). India–Eurasia collision chronology has implications for crustal shortening and driving mechanisms of plates. *Nature* **311,** 615–621.

Pecher, A., (1989). The metamorphism in the Central Himalaya. *Journal of Metamorphic Geology* **7,** 31–42.

Pecher, A. & Le Fort, P., (1986). The metamorphism in Central Himalaya, its relation with the thrust tectonics. *Sciences de la Terre, Memoire* **47,** 285–309.

Perchuk, L. L. & Lavrenteva, I. V., (1983). Experimental investigations of the exchange equilibria in the system garnet–cordierite–biotite. In: Saxena, S. K. (ed.) *Kinetics and Equilibrium in Mineral Reactions*. New York: Springer Verlag, pp. 199–240.

Perkins, D., III & Chipera, S. J., (1985). Garnet–orthopyroxene–plagioclase–quartz geobarometry: refinement and application to the English River Subprovince and the Minnesota River valley. *Contributions to Mineralogy and Petrology* **89,** 69–80.

Pognante, U. & Lombardo, B., (1989). Metamorphic evolution of the High Himalayan Crystallines in SE Zanskar, India. *Journal of Metamorphic Geology* **7,** 9–17.

Ray, S., (1947). Zonal metamorphism in the eastern Himalayas and some aspects of local geology. *Quaternary Journal of Geological Society* **19,** 117–140.

Reddy, S. M., Searle, M. P. & Massey, J. A., (1993). Structural evolution of the High Himalayan gneiss sequence, Langtang valley, Nepal. In: Treloar, P. J. & Searle, M. P. (eds) *Himalayan Tectonics. Geological Society, London, Special Publication* **74,** 375–389.

Robinson, P., Spear, F. S., Schumacher, J. C., Laird, J., Klein, C., Evans, B. W. & Doolan, B. L., (1982). Phase relations of metamorphic amphiboles: natural occurrences and theory. *Mineralogical Society of America, Annual Reviews in Mineralogy* **9B,** 1–227.

Scalliet, B., Pichavant, M. & Roux, J., (1995). Experimental crystallization of leucogranite magmas. *Journal of Petrology* **36,** 663–705.

Searle, M. P. & Rex, A. J., (1989). Thermal model for the Zanskar Himalaya. *Journal of Metamorphic Geology* **7,** 127–134.

Searle, M. P., Cooper, D. J. W. & Rex, A. J., (1988). Collision tectonics of the Ladakh–Zanskar Himalaya. *Philosophical Transactions of the Royal Society of London* **326,** 117–150.

Sengupta, P., Karmakar, S., Dasgupta, S. & Fukuoka, M., (1991). Petrology of spinel granulites from Araku, Eastern Ghats, India, and

a petrogenetic grid for sapphirine-free rocks in the system FMAS. *Journal of Metamorphic Geology* **9,** 451–459.

SinhaRoy, S., (1976). Tectonic evolution of the Darjeeling Himalaya. *Quarterly Journal of the Geological, Mining and Metallurgical Society of India* **48,** 167–178.

SinhaRoy, S., (1982). Himalayan Main Central Thrust and its implications for Himalayan inverted metamorphism. *Tectonophysics* **84,** 197–224.

Spear, F. S., (1991). On the interpretation of peak metamorphic temperatures in the light of garnet diffusion during cooling. *Journal of Metamorphic Geology* **9,** 379–388.

Spear, F. S., (1992). Thermobarometry and *P–T* paths from granulitic rocks: an introduction. *Precambrian Research* **55,** 201–207.

Spear, F. S. & Florence, F. P., (1992). Thermobarometry in granulites. Pitfalls and new approaches. *Precambrian Research* **55,** 209–241.

Staubli, A., (1989). Polyphase metamorphism and development of the Main Central Thrust. *Journal of Metamorphic Geology* **7,** 73–93.

Swapp, S. M. & Hollister, L. S., (1991). Inverted metamorphism within the Tibetan slab in Bhutan: evidence for a tectonically transported heat source. *Canadian Mineralogist* **29,** 1019–1041.

Thakur, V. C., (1986). Tectonic zonation and regional framework of the Eastern Himalaya. *Sciences de la Terre, Memoire* **47,** 347–360.

Thompson, A. B., (1976). Mineral reactions in some pelitic rocks: II Calculation of some *P–T–X* (Fe–Mg) relations. *American Journal of Science* **276,** 401–454.

Treloar, P., Broughton, R. D., Williams, M. P., Coward, M. P. & Windley, B. W., (1989). Deformation, metamorphism and imbrication of the Indian plate, south of the Main Mantle Thrust, north Pakistan. *Journal of Metamorphic Geology* **7,** 111–125.

Van der Molen, I. & Patterson, M. S., (1979). Experimental deformation of partially melted granite. *Contributions to Mineralogy and Petrology* **70,** 218–229.

Vielzeuf, D. & Holloway, J. R., (1988). Experimental determination of fluid-absent melting relations in the pelitic system: consequences for crustal differentiation. *Contributions to Mineralogy and Petrology* **98,** 257–276.

Waters, D. J., (1991). Hercynite–quartz granulites: phase relations and implication for crustal processes. *European Journal of Mineralogy* **3,** 367–386.

Wheeler, J., Treloar, P. J. & Potts, G. J., (1995). Structural and metamorphic evolution of the Nanga Parbat syntaxis, Pakistan Himalayas, on the Indus gorge transect: the importance of early events. *Geological Journal* **30,** 349–371.

Wickham, S. M., (1987). The segregation and emplacement of granite magmas. *Journal of the Geological Society, London* **144,** 281–297.